Characterization Studies of Silicon Photomultipliers: Noise and Relative Photon Detection Efficiency

von

Johannes Schumacher

Bachelorarbeit in Physik

vorgelegt der
Fakultät für Mathematik, Informatik und Naturwissenschaften
der
Rheinisch-Westfälischen Technischen Hochschule Aachen

im Februar 2011

angefertigt am

III. Physikalischen Institut A

betreut durch

Univ.-Prof. Dr. Thomas Hebbeker

Contents

1. Introduction

Astroparticle physics combines the most complex structures of space and the smallest elements; it defines a link between astrophysics and particle physics.

Since the dawn of civilization every culture has scrutinized the star-spangled sky. Elementary questions have been solved, so that nowadays challenges concern ultra-high-energy cosmic rays (UHECR) among others. Several experiments on Earth explore these occurrences.

The southern site of the Pierre Auger Observatory, located near Malargüe, Argentina, is the largest experiment investigating these questions. It joins newest technology and different detector types to determine the origin, mass composition and energy of the studied particles. The Pierre Auger Observatory uses a unique hybrid detection technique for studying extensive air showers initiated by cosmic rays; this technique consists of a surface detector (SD) and a fluorescence detector (FD). Currently, photomultiplier tubes (PMTs) are deployed in FD for the observation of the ultraviolet fluorescence light generated in the extensive air showers.

With new semiconductive, photosensitive devices, these telescopes will work with higher sensitivity. Silicon photomultipliers (SiPMs) have been improved lately. Albeit these photodiodes are rather small, advantages prevail: Compared to the photon detection efficiency (PDE) of current integrated PMTs in FD, silicon photomultipliers will detect more light and therefore more air shower events will be detected. This promises good prospects.

Like every new technology, SiPMs need to be characterized precisely. Since the photon emission flux of the fluorescence light of the air showers is quite low, the thermal noise rate (also known as *dark rate*) has to be analyzed. SiPMs of the newest are quite small; about $9 - 25\,\mathrm{mm}^2$ in size. This necessitates light funnels to concentrate photons from a bigger diameter to a smaller area.

Thereby, light which enters the Winston cone vertically will not exclusively hit the SiPM vertically. The angular dependent efficiency has to be measured and compared with expectations to permit the usage of a combination of cone and SiPM.

The topic of this thesis is to evaluate the angular dependency of the photon detection efficiency and the study of the *dark rate*.

Outline

A brief glimpse in the structure of the Pierre Auger Observatory shall motivate these characterization studies of silicon photomultipliers (chapter 2).

These studies require profound knowledge of theoretical foundations. Since this thesis is not a course-book of semiconductor physics, this part is kept to a short and strict minimum (chapter 3).

The first experiment deals with the noise rate, induced by thermal excitation (chapter 4).

The efficiency of a system of a light funnel (here Winston cone) and a silicon photomultiplier is part of the last section (chapters 5 and 6).

Finally, results are summarized and a brief outlook is given, representing latest developments at the RWTH Aachen University, concerning silicon photomultipliers at the Pierre Auger Observatory.

2. Cosmic Rays and the Pierre Auger Observatory

Ultra-high-energy cosmic rays (UHECR) are particles with an energy up to 10^{20} eV with unknown sources; they can create a first reaction with nuclei (e.g. nitrogen) in the atmosphere creating new *secondary particles*. These particles interact with the atmosphere as well or decay producing a cascade of secondary particles. This is called an *extensive air shower*. Charged secondary particles can excite the nitrogen molecules in the atmosphere which emit fluorescence light in the ultraviolet and blue-visible frequency range while de-exciting. This spectrum is shown in figure 2.1. It is possible to observe these photons.

Due to the low event-flux of e.g. 1 particle per km^2 and century at an energy of about 10^{20} eV, the instrumented area needs to be large [2]. The southern site of the Pierre Auger Observatory hosts 1600 surface detector (SD) stations with a distance of 1.5 km to the next neighbor, at a region of about 3000 km^2. Consisting of three photomultiplier tubes (PMT) and twelve tons ultra-pure water, SD stations

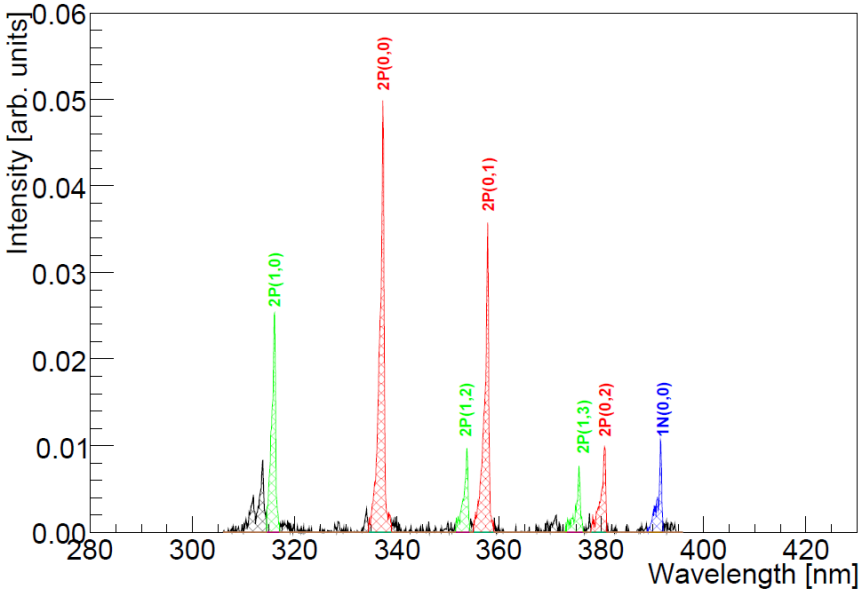

Figure 2.1: Almost discrete nitrogen fluorescence spectrum in dry air at 1013 hPa emitted by an extensive air shower in the range of ultraviolet light [1].

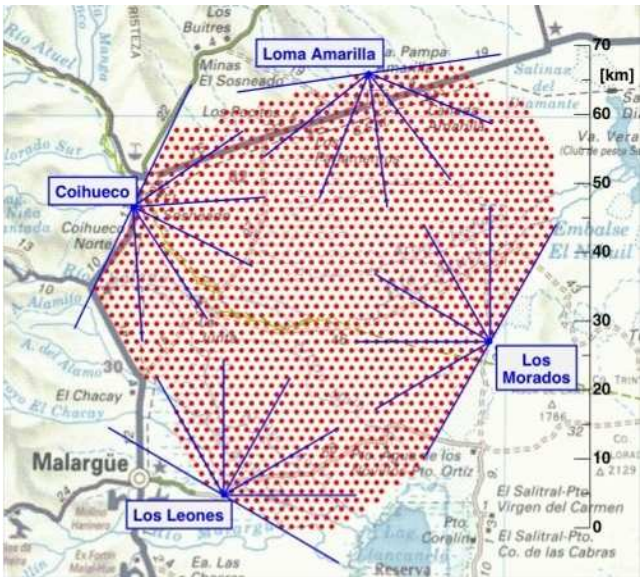

Figure 2.2: Map of the Pierre Auger Observatory near Malargüe, Argentina [3]. Each red dot represents a SD station. Blue lines stand for the field of view of the fluorescence telescopes.

detect Cherenkov light emitted by secondary particles in the water. In addition, four buildings hosting six telescopes each overlook the area at its edge, see figure 2.2. Since each fluorescence telescope has a field of view of $30° \times 30°$, each building has an active azimuth of 180°. A hybrid event detected by SD and FD is shown in figure 2.3.

The camera of a fluorescence telescope consists of an array of 440 PMTs. Mirrors reflect the emitted light right onto these photosensitive devices. Showers can only be detected at dark nights, which yields a duty cycle of FD of about $10\% - 15\,\%$.

Today's silicon photomultipliers promise a better light detection, due to a higher photon detection efficiency (PDE), than currently used PMTs in FD.

Since the functionality of these devices differ from the theory of PMTs, some background knowledge is necessary, to understand advantages and disadvantages of silicon photomultipliers.

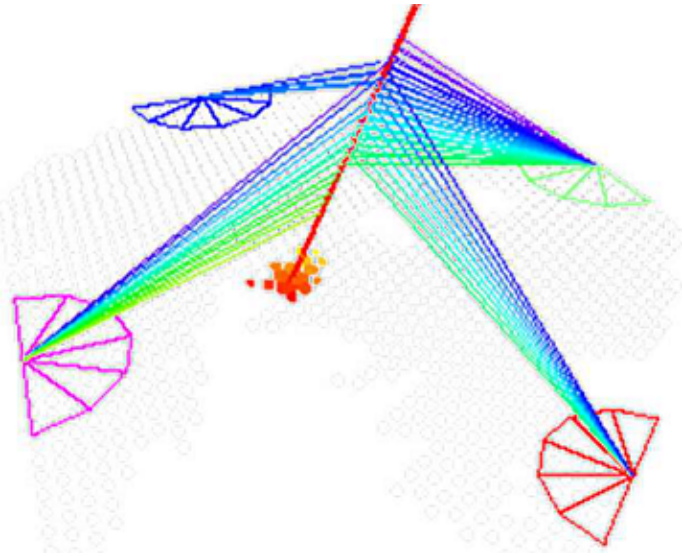

Figure 2.3: A hybrid event. FD (pie charts in the corner) and SD (red circles) reconstruct an air shower event (red axes in the middle) [3]. Time information is color-coded. Dot-size (SD) increases with energy measured in this station.

3. New Methods in Light Detection

This chapter deals with the theoretical foundations of silicon photomultipliers. In order to understand why these devices overcome traditional photomultiplier tubes, knowledge of the detection principle is required. The described methods culminate in the signal processing technique and the devices that are used to determine the characteristics of silicon photomultipliers.

3.1 Photodiode and Silicon Photomultiplier

Photodiode (PD)

Doped semiconductors, used as photoconductive devices, reduce their internal resistance from R_{D} (dark resistance) to R_{I} (illuminated resistance) on irradiation. An external power source is applied, which yields an electric field E, within the intrinsic space region. These detectors are called photodiodes (PDs).

In undoped semiconductors, photons with an energy $E_\gamma = h \cdot \nu \geq \Delta E_{\mathrm{g}}$ excite electrons from the valence band into the conduction band. Here, ΔE_{g} is the band-gap energy difference. In p-doped and n-doped semiconductors photons with an energy greater than ΔE_{d} and ΔE_{a} are absorbed, respectively, see figure 3.1. These energy-gaps are essentially smaller than the band-gap of the semiconductor, which allows detection of photons with lower energies. However, this requires low temperatures

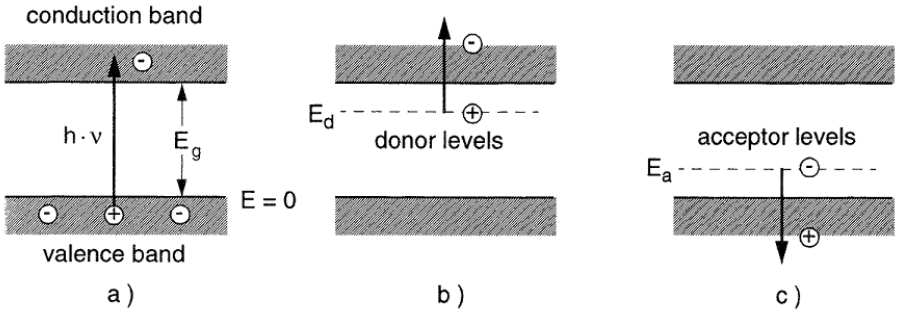

Figure 3.1: Photoabsorption in undoped semiconductors (a) and by donors (b) and acceptors (c) in n- or p-doped semiconductors [4].

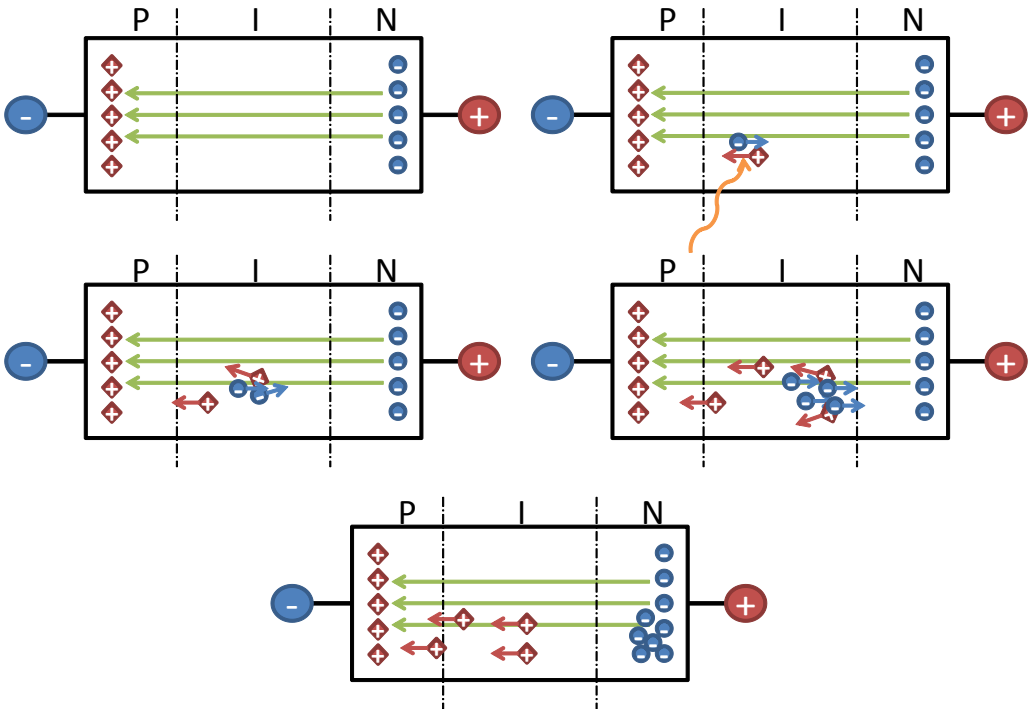

Figure 3.2: Visualized avalanche-process within an Avalanche Photodiode (APD). The order is to be read from left to right and top to bottom. Green arrows stand for the electric field E within the pn-junction, induced by an applied voltage V_{OP} (see text for details).

of about $T \leq 10\,\mathrm{K}$ to reduce thermal excitation of electrons satisfactorily. When the photodiode is illuminated, the output voltage changes with

$$\Delta V_{\mathrm{out}} = \left(\frac{R_{\mathrm{D}}}{R_{\mathrm{D}} + R} - \frac{R_{\mathrm{I}}}{R_{\mathrm{I}} + R} \right) \cdot V_0, \tag{3.1}$$

where V_0 corresponds to the bias-voltage [4]. ΔV_{out} is maximized for $R = \sqrt{R_{\mathrm{D}} \cdot R_{\mathrm{I}}}$. This effect is referred to as a *fired cell*.

Avalanche Photodiode (APD)

Compared to photodiodes, APDs use free negative charged carriers, which gain enough energy in the accelerating field E to create electron-hole pairs themselves. This process is visualized in figure 3.2.

Reverse-biased diodes can achieve amplification of the signal up to $50 - 200$ compared to regular photodiodes. This gain increases with the operating voltage V_{OP}. A circuit of an APD is shown in figure 3.3.

Only electrons produce avalanches by creating additional electron-hole-pairs. While these electrons have reached the anode of the diode, holes drift to the cathode more slowly, due to a lower mobility. If these carriers are additionally used for the avalanche process, the photodiode may gain much higher amplifications, which is known as Geiger-mode operation.

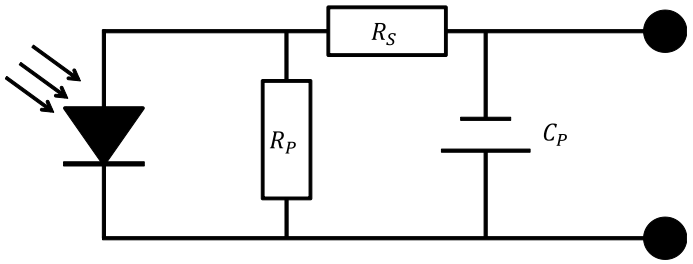

Figure 3.3: Equivalent circuit diagram of an avalanche photodiode - reprinted from [4].

Geiger-mode Avalanche Photodiode (G-APD)

Most avalanche photodiodes are operated in Geiger-mode. G-APDs have been improved at the beginning of the 21th century [5]. Amplification of $10^5 - 10^7$ is possible. Avalanches created by holes are intentionally used to amplify the input signal. Therefore a high-ohmic resistor is necessary to discharge the photodiode and stop the avalanche. The time that is needed for this process is called the *recovery time* of the photodiode. The amplification A is proportional to the overvoltage $V_{\mathrm{OV}} = V_{\mathrm{OP}} - V_{\mathrm{BD}}$, which is the difference between operating voltage and breakdown voltage and thus given by

$$A \propto C\,/\,q \cdot V_{\mathrm{OV}} = C\,/\,q \cdot \left(V_{\mathrm{OP}} - V_{\mathrm{BD}}\right). \tag{3.2}$$

V_{BD} delivers the minimal needed *energy* to start an avalanche process. This value depends on the temperature, see chapter 4; C is the capacitance of the APD, and q the charge of the electron. Single photons can create signals of several mV at a $50\,\Omega$ load [5].

The detection rate of avalanche photodiodes does not exceed one photon at the same time. This can be expended by connecting several APDs in parallel.

Silicon Photomultiplier (SiPM)

Silicon photomultipliers are arrays of 100-1000 Geiger-mode avalanche photodiodes. The geometric fill-factor g is given by the size of each photodiode A_{CELL} (in further context: *cell*), their number N and the spacing between neighboring cells d:

$$g = \frac{A_{\mathrm{CELL}}}{\left(\sqrt{A_{\mathrm{CELL}}} + \frac{N-1}{N} \cdot d\right)^2}. \tag{3.3}$$

This affects the photon detection efficiency intensively. Considering the circuit of a common silicon photomultiplier (figure 3.4), it is obvious that the generated photocurrent is proportional to the number of fired cells, according to Kirchhoff's circuit law. This results in the observed output signal (hence each cell needs time to rise and recover), see figure 3.5.

Electron-hole-pairs can be randomly created by thermal excitation. This is a major drawback of silicon photomultipliers and is called *dark rate* or *thermal noise rate*.

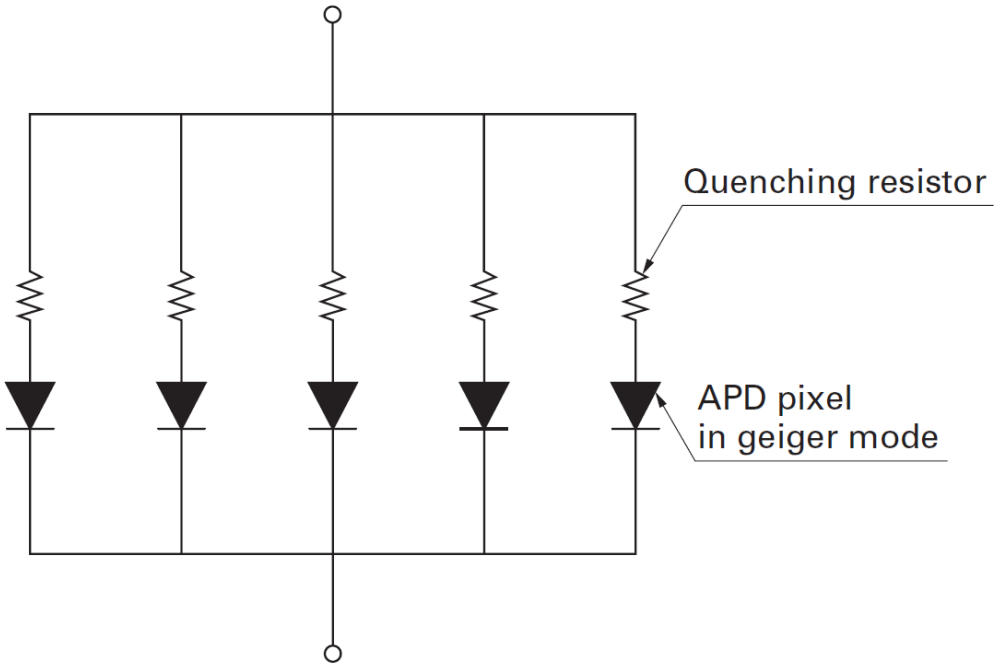

Figure 3.4: Equivalent circuit diagram of a silicon photomultiplier - Each diode represents a (Geiger-mode) avalanche photodiode (see figure 3.3) - taken from [6].

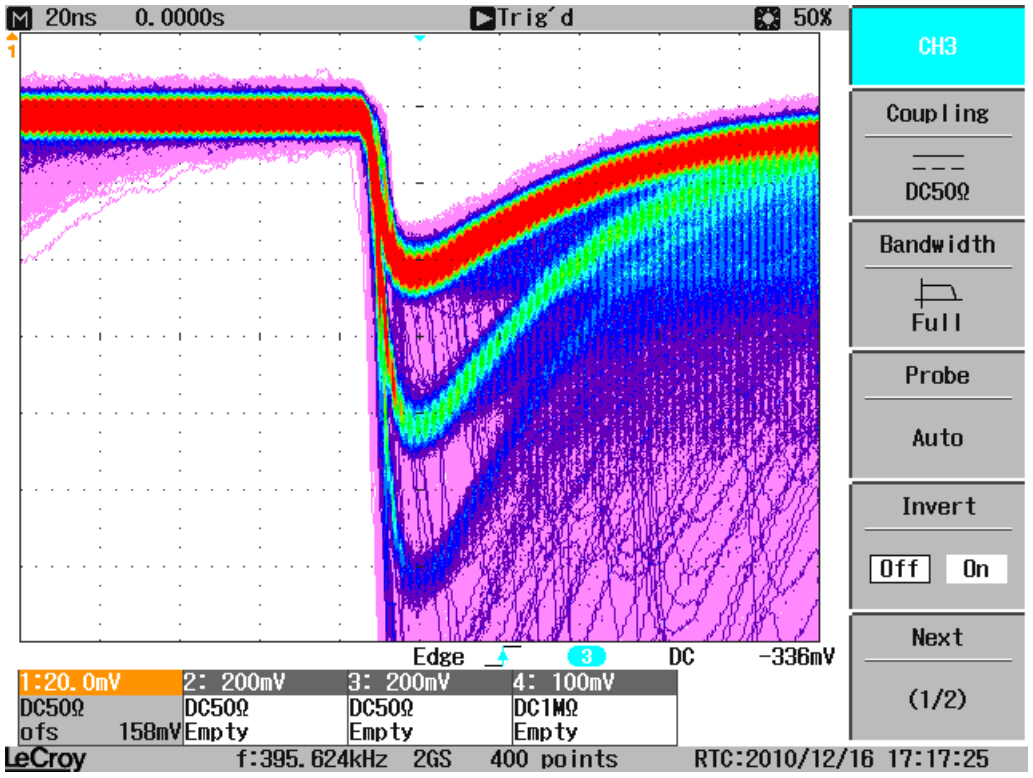

Figure 3.5: Amplified noise signal of a silicon photomultiplier - Screenshot printed via LeCroy Wavejet 354A oscilloscope at a 50 Ω load. Horizontal axis represents time (1 div ≙ 20 ns), vertical axis represents voltage (1 div ≙ 20 mV). The event rate is color coded.

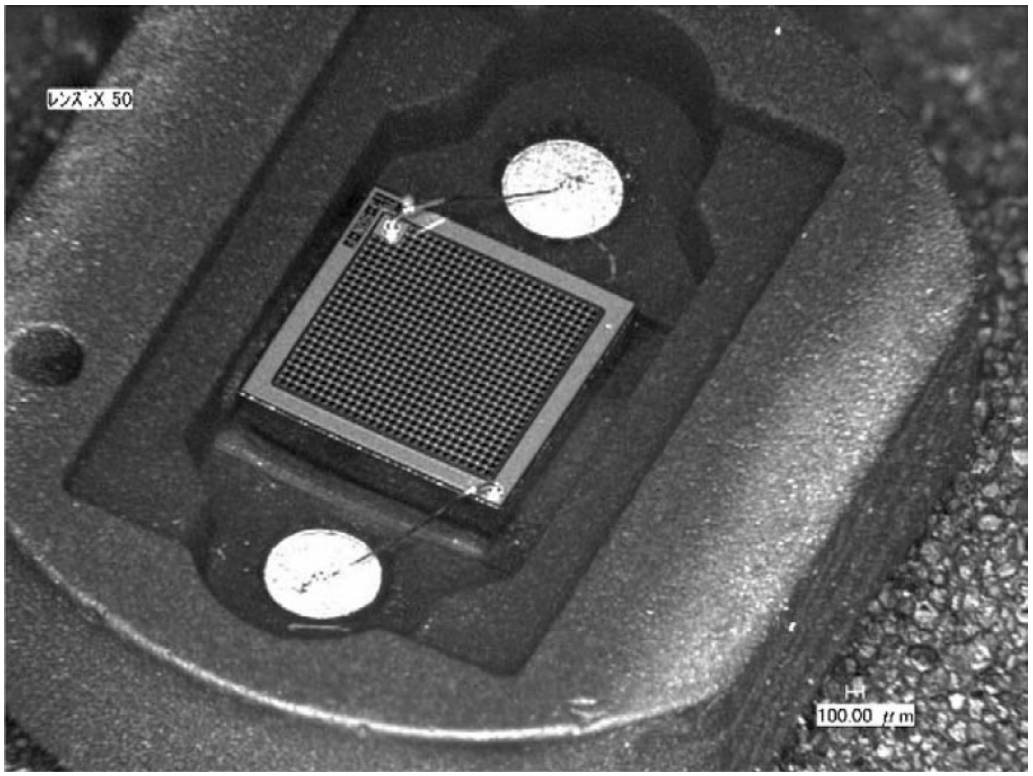

Figure 3.6: Microscope image of HAMAMATSU S103612-11-100C silicon photomultiplier [8]. The sensitive area in the middle is $1 \times 1\,\mathrm{mm}^2$ in size.

Thermally created carriers gain enough energy through electric amplification to produce avalanches themselves. This signal is identical to photon induced processes. In general parlance, the SiPM mistakes thermal excitation for photons. Evidently, the *dark rate* has to be measured for different temperatures (see chapter 4).

The S103612-11-100C is the SiPM type that is used in this bachelor thesis. It is manufactured by HAMAMATSU and consists of a matrix of 10×10 cells, covering an area of $1\,\mathrm{mm}^2$, see figure 3.6. Hamamatsu maintains, that their silicon photomultipliers of this charge have a fill-factor of $g = 78.5\%$. This can be expressed in cell-size $A_{\mathrm{cell}} = 7.85 \times 10^{-3}\,\mathrm{mm}^2$ and cell-to-cell distance $d = 1.15\,\mu\mathrm{m}$ [7].

Particularized noise events are *optical crosstalk* and *afterpulses*: Free carriers may recombine with their counterparts and create photons that can be detected by other *cells*. An additional photon event is generated. This effect is called optical crosstalk. The term afterpulses refers to electrons and holes that are hindered of reaching the anode and cathode, respectively, due to lattice scattering. These carriers may be released afterwards and create photon events through avalanche production.

The spacing d is added to reduce optical crosstalk and to host the quenching resistors, see figure 3.7. The maximal photon detection efficiency (PDE), including crosstalk and afterpulses, at the peak sensitivity wavelength $\lambda_p = 440\,\mathrm{nm}$ is stated to be around 65%. Of course, crosstalk and afterpulse events have to be subtracted, but this is not part of this bachelor thesis. The important specifications given by the manufacturer are printed in table 3.1.

Property	Value
Number of pixels	100
Fill factor	78.5%
PDE (at $\lambda_p = 440\,\mathrm{nm}$)	65%
Dark count /kHz	$600 - 1000$
Gain	2.4×10^6

Table 3.1: SiPM type S103612-11-100C information provided by HAMAMATSU [7].

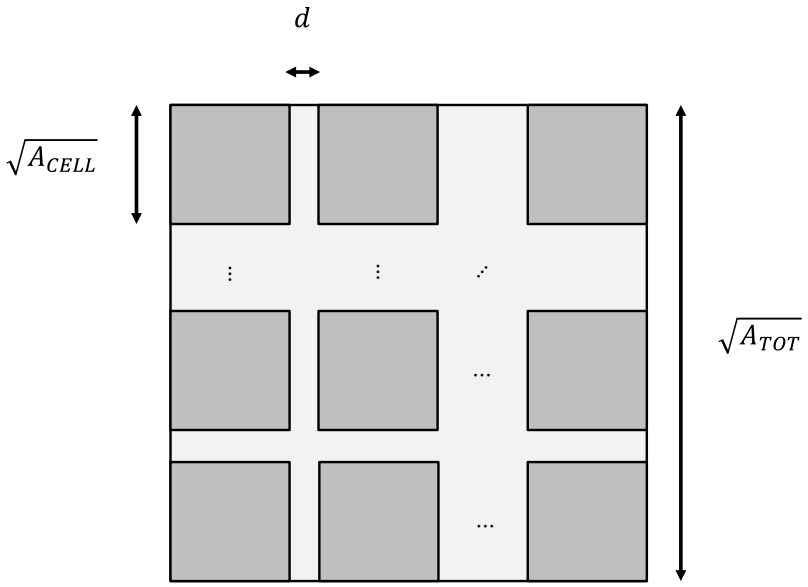

Figure 3.7: Silicon photomultiplier - Pattern - Dark grey: Active area - Light grey: Spacings for quenching resistors and optical crosstalk reduction, cf. figure 3.6.

3.2 Signal Processing

3.2.1 MPPCC 2.0

MPPCC is a frontend electronics board for amplification of the SiPM signals and output via two LEMO 00 connectors. A small part of this device can be seen in figure 3.8, beneath the coatings and the silicon photomultiplier.

First output, also known as *int out*, is intended to be used for energy measurements, since signals are integrated. For second output, signals are emitted individually (time measurements) and therefore called *fast out*. This output is used further on.

The board contains a temperature sensor MAXIM DS18B20 [9]. The applied voltage can be regulated temperature-dependent. This feature has been disabled for experiments in the bachelor thesis. The sensor is used for temperature regulation and controlling. Its measurement uncertainty is given as

$$\Delta T = \pm 0.5\,^{\circ}\mathrm{C}, \tag{3.4}$$

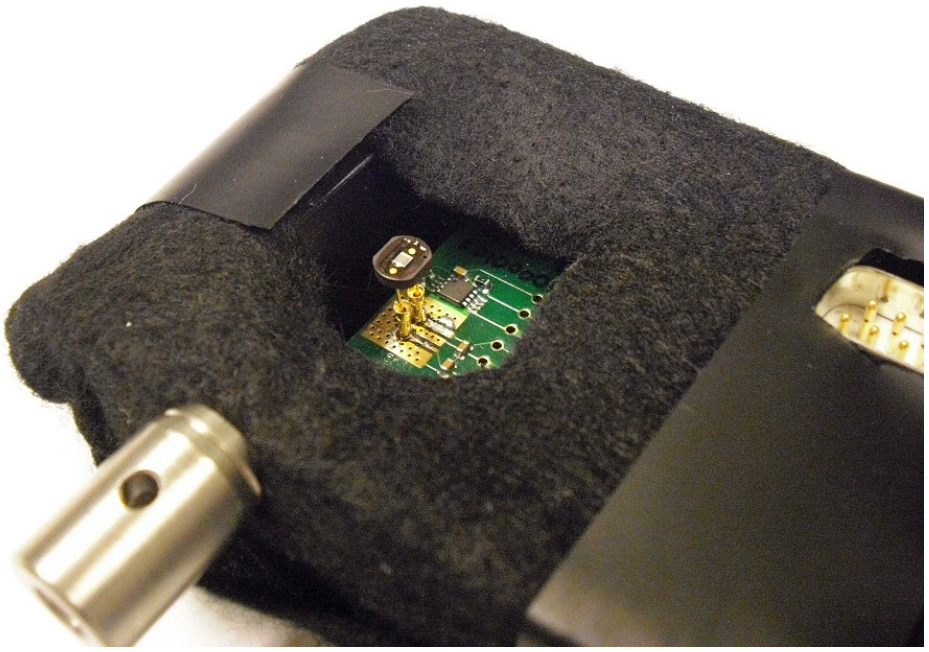

Figure 3.8: Frontend electronics designed by F. Beißel (III. Phys. Inst. B, RWTH Aachen University) and silicon photomultiplier manufactured by Hamamatsu (HAMAMATSU S103612-11-100C) conditioned for the relative PDE measurement.

for measurement range between -10 °C and +85 °C.

Mppcc has been designed and manufactured by F. Beißel, III. Phys. Inst. B, RWTH Aachen University, Germany.

3.2.2 CAEN V965 - 16/8 Channel Dual Range QDC

Caen V965 is a 16-channel Charge-to-Digital Converter, integrating current of negative inputs [10]. These inputs are analyzed by two ADCs (Amplitude-to-Digital Converter) in parallel, performing a 1x (LRC) or 8x (HRC) gain stage, which yields two different output data. High Range Channel (HRC) features output from 0 to 900 pC. Low Range Channel (LRC), however, emits data from 0 to 100 pC. Since bin-count stays the same for HRC and LRC, the Low Range Channel has a resolution higher than the High Range Channel. LRC is used for small amplitudes in current and proper resolution, whereas HRC is used for bigger amplitudes with less need for high resolutions. A common SiPM QDC output is shown in figure 5.5 on page 34. Additional information can be obtained from CAEN documentation [10].

3.2.3 Wiener VM-USB 2.0 Bridge

Wiener VM-USB is an USB-interface for signal transmission between the hardware itself, e.g. QDC and data acquisition devices, like Personal Computers (PC) with USB-support [11].

A Master-Control interprets data from the VME-bus-interface in serial data streams (FIFO-mode). Appropriate stream-reader for direct access (read and write) have been written at III. Phys. Inst., RWTH Aachen, Germany and combined into a C++ library, called liblab [12].

3.2.4 LeCroy Wavejet 354A - 500 MHz Oscilloscope

LeCroy Wavejet 354A is a digital oscilloscope that is able to be controlled remotely via USB and/or 10/100BaseT RJ-45 Ethernet connection. Vertical gain accuracy is $\pm\,(1.5\% + 0.5\% \cdot \text{full-scale})$. Since the oscilloscope is operated with a 50 mV/div vertical sensitivity for trigger measurement and 20 mV/div vertical sensitivity for base-line measurement, the expected accuracy will be

$$\begin{aligned} \Delta V_{\text{TRIG}} &= \pm\,(1.5\% \cdot V_{\text{SIG}} + 0.5\% \cdot 50\,\text{mV/div} \cdot 8\,\text{div}) \\ &= \pm\,(1.5\% \cdot V_{\text{SIG}} + 2.0\,\text{mV})\,, \end{aligned} \tag{3.5}$$

$$\begin{aligned} \Delta V_{\text{BASE}} &= \pm\,(1.5\% \cdot V_{\text{SIG}} + 0.5\% \cdot 20\,\text{mV/div} \cdot 8\,\text{div}) \\ &= \pm\,(1.5\% \cdot V_{\text{SIG}} + 0.8\,\text{mV})\,. \end{aligned} \tag{3.6}$$

The horizontal accuracy (timebase) is typically given as

$$\Delta t \leq 1\,\text{ns}. \tag{3.7}$$

Important features of the LeCroy Wavejet 354A are Measure and Math functions. The dark rate can therefore be measured directly, using the Frequency function [13].

3.2.5 Power Supplies

Keithley Sourcemeter 2400 - Digital Power Supply

Keithley Sourcemeter 2400 is a digital power supply, providing measurement functions for applied voltages and current [14]. This device may be controlled remotely via RS-232 connection; better known as serial COM-port. Voltages can be get and set programmatically. The measurement ranges have not been changed during the experiment, which yields uncertainties (at $T = (23 \pm 5)$ °C) of

$$\begin{aligned} \Delta V_{\text{GET}} &= \pm\,(0.015\% \cdot V_{\text{GET}} + 0.01\,\text{V}) \\ \Delta V_{\text{SET}} &= \pm\,(0.02\% \cdot V_{\text{SET}} + 0.024\,\text{V})\,, \end{aligned} \tag{3.8}$$

$$\begin{aligned} \Delta I_{\text{GET}} &= \pm\,(0.031\% \cdot I_{\text{GET}} + 0.02\,\mu\text{A}) \\ \Delta I_{\text{SET}} &= \pm\,(0.025\% \cdot I_{\text{SET}} + 0.006\,\mu\text{A})\,. \end{aligned} \tag{3.9}$$

V_{SET} is equivalent to the operational voltage V_{OP} that has been set. V_{GET} on the other hand, is the voltage that is measured by KEITHLEY SOURCEMETER 2400 afterwards. The same applies to I_{SET} and I_{GET}.

Lambda ZUP-10-20 - Programmable Power Supply

Since the LAMBDA ZUP-10-20 is used for power supply of the frontend board only, it is not necessary to provide additional information about this device at that point. For completeness, however, the approx. accuracy is given as

$$\Delta V_{\mathrm{DC}} = \pm\,(0.02\% \cdot V_{\mathrm{DC}} + 0.008\,\mathrm{V})\,. \tag{3.10}$$

Here V_{DC} is always $\pm\,5\,\mathrm{V}$. These electronics feature a built-in RS-232 interface, which allows remote access. [15]

3.2.6 Cooling Chamber

The Cooling Chamber COOLI was part of a diploma thesis at III. Phys. Inst. B, RWTH Aachen University, Germany, originally constructed for testing silicon strip detectors for the inner tracker of CMS-detector [16].

The temperature can be regulated remotely via Ethernet connection in range of -20 °C to +30 °C. Dry air flushing reduces condensate at low temperatures. Cooling is achieved through several Peltier elements, fixed within the cooling box. Synthetic material is used for lagging and copper foil decreases electromagnetic disorders.

The cooling chamber dissipates heat to the in-house cooling water system.

This device is used for monitoring the temperature through the MPPCC temperature sensor and for keeping the temperature steady. Additional information about this box can be retrieved from the diploma thesis [16].

3.2.7 LED

L-7113UVC LED manufactured by KINGBRIGHT has been used to produce light pulses. The wavelength given by the manufacturer is $\lambda \approx 400\,\mathrm{nm}$, see figure 3.9. This is quite more blue light than ultra-violet, but according to the spectrum shown in figure 2.1 from chapter 2 on page 3 the frequency is near the fluorescence spectrum of nitrogen.

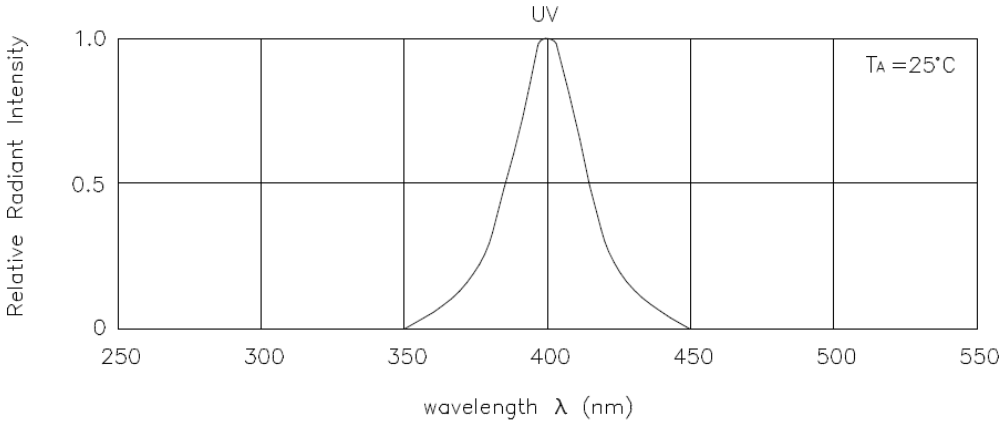

Figure 3.9: Relative intensity vs. wavelength of KINGBRIGHT L-7113UVC LED [17].

4. Thermal Noise Rate

One of the fundamental characteristics of thermal sensitive devices to be determined is the noise rate. The descent of thermal-induced noise events is described in chapter 3.

To be able to distinguish between photo-events and noise in future applications, a threshold has to be set higher than the noise itself and lower than the photon-produced signal. Therefore, it is necessary to determine the thermal noise rate and assure, that the photo-signal exceeds this value. Otherwise, light cannot be detected sufficiently, e.g. the photon flux is too low.

FD electronics are held temperature-stable. The experimental setup represents this environment. Since air conditioning regulates the temperature in FD, the climate is monitored, too.

4.1 Experimental Setup

Figure 4.1 shows a pattern of the experimental setup. The setup has to be completely cleared of external light. The temperature has to be kept at a steady state during the time of measurement. As the temperature dependency of the noise rate is a topic of this thesis the temperature control is a main concern. The cooling box can be used as both, a protection against light and a temperature regulator, see chapter 3.

The silicon photomultiplier is adjusted on the frontend board MPPCC and placed in the cooling box. This frontend electronics contains a temperature sensor, which needs to be calibrated beforehand, see section 4.1.1.

Connection for fast output is plugged to LeCroy Wavejet 354A - digital oscilloscope, which can be controlled remotely via an Ethernet connection. The power of the silicon photomultiplier is supplied by Keithley 2400 Sourcemeter. This device is able to measure the operating voltage V_{OP} and the active current I (chapter 3). All settings and calibrations can be operated remotely.

4.1.1 Temperature Calibration

The temperature has been calibrated in the first place. A calibrated P470 temperature sensor has been installed for this purpose [18]. Its absolute uncertainty is stated to be 0.5 °C. Direct comparison between the built-in sensor MPPCC and the P470 can be seen in table 4.1.

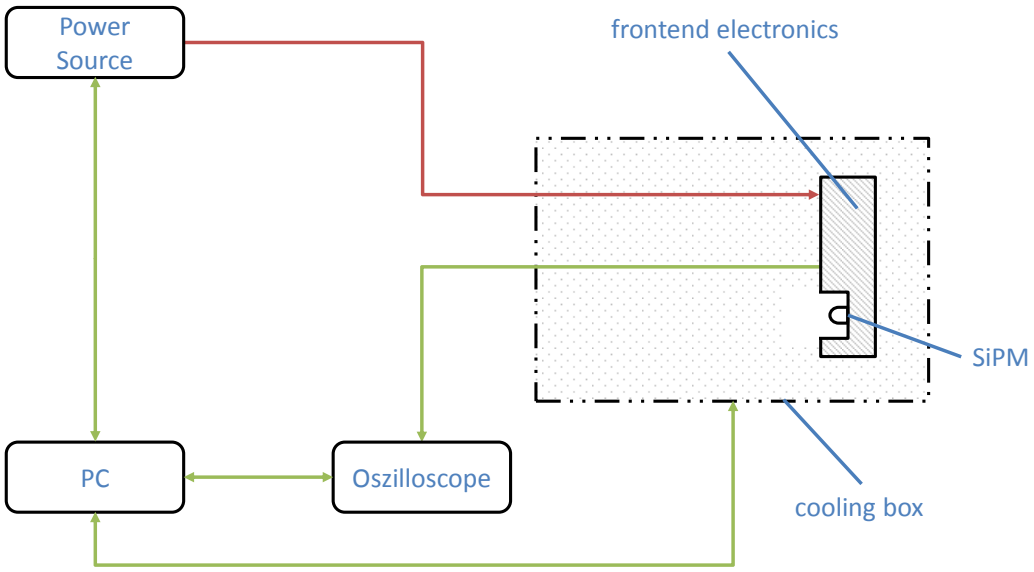

Figure 4.1: Experimental Setup - Data acquisition cables are marked in green, power source is tagged in red, see text for details.

T_{MPPCC} / °C	T_{P470} / °C
21.3 ± 0.5 (syst.)	18.9 ± 0.5 (syst.)
16.2 ± 0.5 (syst.)	13.6 ± 0.5 (syst.)
16.1 ± 0.5 (syst.)	13.6 ± 0.5 (syst.)
10.6 ± 0.5 (syst.)	8.1 ± 0.5 (syst.)
5.2 ± 0.5 (syst.)	2.6 ± 0.5 (syst.)

Table 4.1: Comparison between temperature sensors: MPPCC-sensor and calibrated P470. No statistical fluctuations have been measured here. Systematic errors are explained in chapter 3.

This sensor is used to specify the calibrated temperature coefficient (difference) δT. After the calibration tests this sensor was not needed anymore, thus speeding up further measurements since the temperature T_{MPPCC} can be controlled remotely. The temperature coefficient is then given by

$$\delta T = T_{\mathrm{MPPCC}} - T_{\mathrm{P470}} = (2.52 \pm 0.04\,(\mathrm{stat.}))\ ^{\circ}\mathrm{C}. \tag{4.1}$$

T_{MPPCC} can be measured and is retrieved remotely via Ethernet connection, see chapter 3. This leads to the temperature

$$\begin{aligned} T = (T_{\mathrm{MPPCC}} - \delta T) \pm \sqrt{\Delta^{\mathrm{stat.}} T_{\mathrm{MPPCC}}^2 + \Delta^{\mathrm{stat.}} \delta T^2} \\ \pm \Delta^{\mathrm{syst.}} T_{\mathrm{MPPCC}} \pm \Delta^{\mathrm{syst.}} T_{\mathrm{P470}}. \end{aligned} \tag{4.2}$$

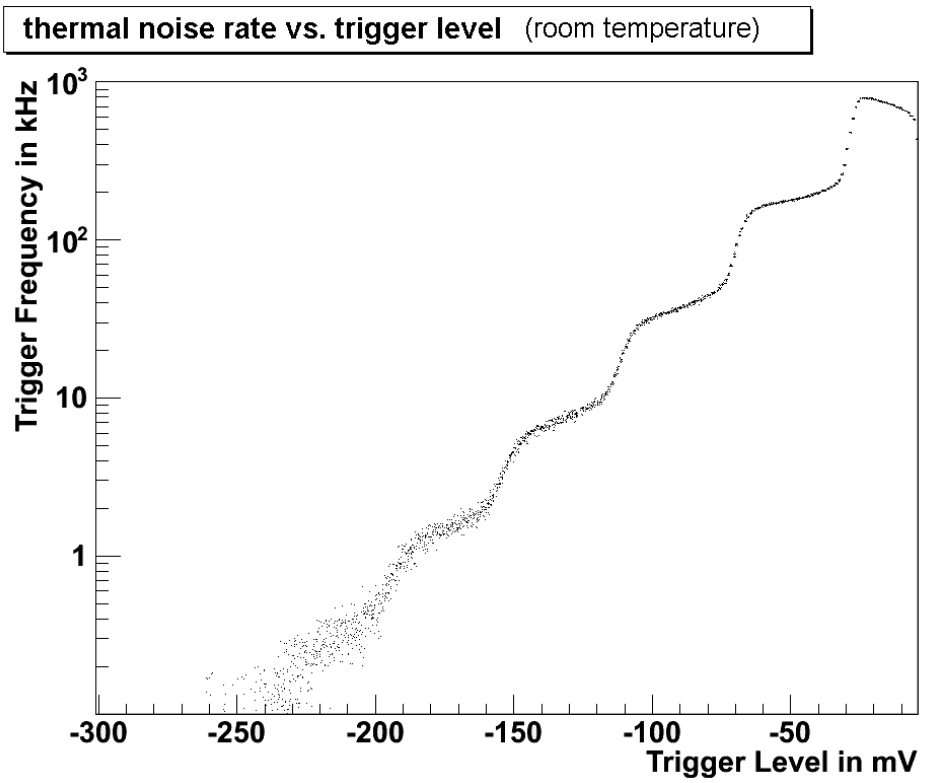

Figure 4.2: Thermal noise rate vs. threshold (trigger level in mV) at room temperature and $V_{\mathrm{OP}} = (71.00 \pm 0.02\,(\mathrm{syst.}))$ V.

$\Delta T_{\mathrm{MPPCC/P470}}$ are the statistical and systematical uncertainties on $T_{\mathrm{MPPCC/P470}}$, see chapter 3. [19]

4.2 Analysis

4.2.1 First Run

As a first approach, the thermal noise rate is measured for various trigger levels at room temperature and $V_{\mathrm{OP}} = (71.00 \pm 0.02\,(\mathrm{syst.}))$ V to assure data acquisition correctly, see figure 4.2. The plot meets the expectation, see chapter 3.

Its characteristic steplike form is unique [5] [20] [21], since the number of fired cells is discrete and is equivalent to the number of detected photons. At a given threshold of 0.5 p.e. (p.e. = photon equivalent), the measured noise rate is about $f^{\mathrm{noise}}_{\mathrm{MEAS}}(0.5\,\mathrm{p.e.}) \approx 800\,\mathrm{kHz}$. The manufacturer specifies a thermal noise rate of $f^{\mathrm{noise}}_{\mathrm{HAM}}(0.5\,\mathrm{p.e.}) = 576\,\mathrm{kHz}$ at the same threshold, but at a temperature of 25 °C and $V_{\mathrm{OP}} = 70.79\,\mathrm{V}$.

So, the noise rate does apparently not increase with increasing temperature, which may refute theory, chapter 3, assuming room temperature beneath 25 °C. This phenomenon is analyzed in further context.

The next step is a temperature variation. The operating voltage is kept steady. Figure 4.3 shows the result of this measurement.

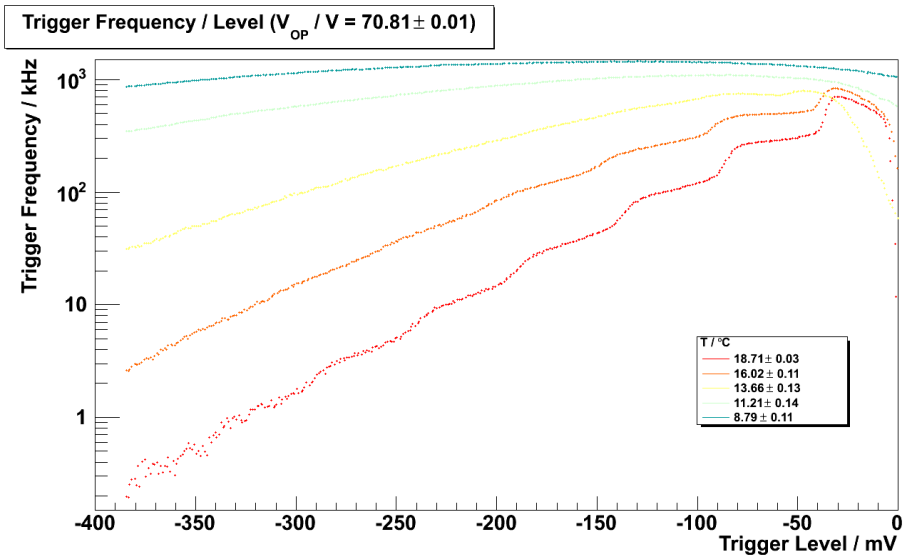

Figure 4.3: Thermal noise rate vs. threshold (trigger level in mV) at various temperatures and $V_{\mathrm{OP}} = (70.81 \pm 0.02\,(\mathrm{syst.}))$ V.

At first glance the results are not expected, since the overall noise rate apparently increases with decreasing temperature. To understand this phenomenon, additional theory is necessary.

The overvoltage $V_{\mathrm{OV}} = V_{\mathrm{OP}} - V_{\mathrm{BD}}$ is equivalent to the difference between the operating voltage V_{OP} (which is the applied voltage), and the breakdown voltage V_{BD}. The voltage, at which the electrons gain enough energy to produce an avalanche is called the breakdown voltage. This value increases with temperature linearly [20]. So, the overvoltage has to be maintained constant, which means, that the applied operating voltage $V_{\mathrm{OP}} = V_{\mathrm{OV}} + V_{\mathrm{BD}}$ needs to be varied. To do this, V_{BD} has to be determined first.

4.2.2 Determination of the Breakdown Voltage

We have seen, that the value of the breakdown voltage is essential for direct comparison of the noise rate between various temperatures. The general idea behind the method, described explicitly in this section, is the determination from the I-V_{OP}-diagrams.

The theory states, that at a certain value of the operating voltage, the current will rise exponentially. This point is the breakdown voltage. If we then plot the temperature versus the breakdown voltage, the slope β [mV/K] can be obtained. This value indicates, how much the overvoltage V_{OV} differs with the temperature [21].

I-V_{OP}-diagrams
Since the power source is controlled remotely, it is quite easy to gather the current I for different operating voltages V_{OP}. Both parameters have been measured for 10

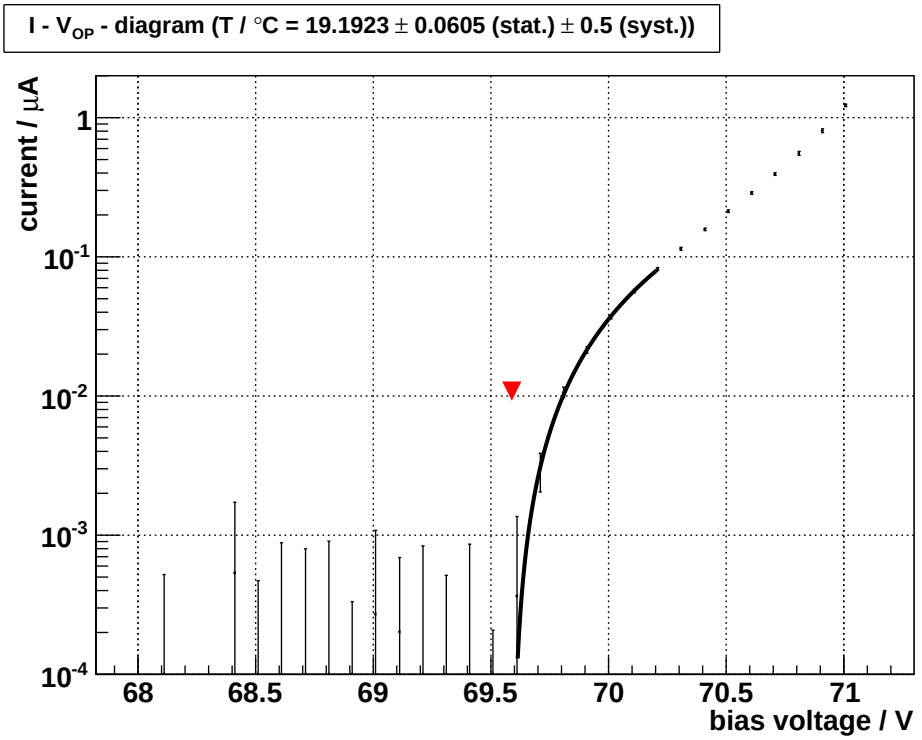

Figure 4.4: Silicon photomultiplier HAMAMATSU S103612-11-100C - current vs. operating voltage at temperature $T = (19.19 \pm 0.06\,(\text{stat.}) \pm 0.50\,(\text{syst.}))\,^{\circ}\text{C}$. The red triangle marks the breakdown voltage for this temperature

seconds each, to determine statistical fluctuations. A resulting plot can be seen in figure 4.4. Note the logarithmic scale for the current.

Due to resonances and oscillating events, see figure 3.5, at high overvoltage $V_{\text{OV}} \geq 2\,\text{V}$, the plots of the I-V_{OP}-diagrams have a slight inflection point, see also [8]. Therefore, fits have to be made carefully. A cut is applied at the data right before the dip to reduce uncertainties. The first data-points are used to fit a 1^{st}-order polynomial. This is the leakage current I_{leak}, which streams in reverse-biased diodes below the breakdown voltage. Finally, a polynomial of 2^{nd} order is fitted on the data beyond the breakdown voltage. Each boundary is determined programmatically, since they are quite easy to be estimated analytically [20].

An exponential fit results in a slightly higher uncertainty. This phenomenon is described in various literature, e.g. [21] and not yet fully understood. However, the intersection between the linear and the quadratic fit is the point of the breakdown voltage for this specific temperature.

The method used in this thesis utilizes a linear fit, which is subtracted from the data; the vertex of the quadratic function is equal to the breakdown voltage for this temperature, see figure 4.4. A linear regression leads to

$$V_{\text{BD}}(T) = \beta \cdot T + V_{\text{BD}}(0\,^{\circ}\text{C}). \tag{4.3}$$

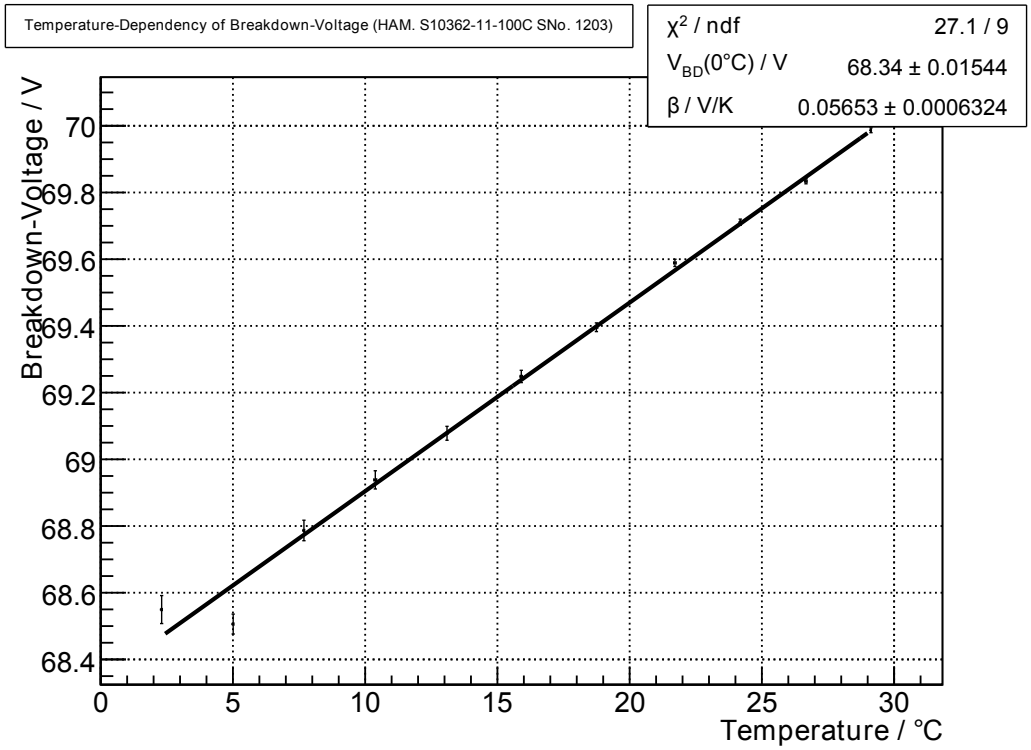

Figure 4.5: Temperature dependency of the breakdown voltage of SiPM-type Hamamatsu S103612-11-100C.

V_{BD}-slope

The method described above is applied on any temperature data available. The individual values for $V_{\mathrm{BD}}(T)$ are plotted in figure 4.5 (pol2). A linear fit retrieves the slope for the increase of the temperature dependency of the breakdown voltage, according to equation (4.3).

To minimize errors on this value, χ^2 /ndf is optimized. Therefore, low-temperature data has been removed. This can be seen in figure 4.5 to 4.7.

This yields the following values for β;

$$\beta^{\mathrm{pol2}} = (55.70 \pm 0.74)\ \mathrm{mV/K} \qquad V_{\mathrm{BD}}^{\mathrm{pol2}}(0°\mathrm{C}) = (68.36 \pm 0.02)\ \mathrm{V} \tag{4.4}$$

$$\beta^{\mathrm{HAM}} = 56\,\mathrm{mV/K} \tag{4.5}$$

$V_{\mathrm{BD}}^{\mathrm{HAM}}(0\,°\mathrm{C})$ is not specified. For further analysis, β^{pol2} is used. Hamamatsu indicates the temperature coefficient β^{HAM} of the reverse voltage for any SiPM of this charge. The measured slopes nicely fit these indications.

4.2.3 Second Run

This section deals with the effects of the overvoltage to the signals of silicon photomultipliers.

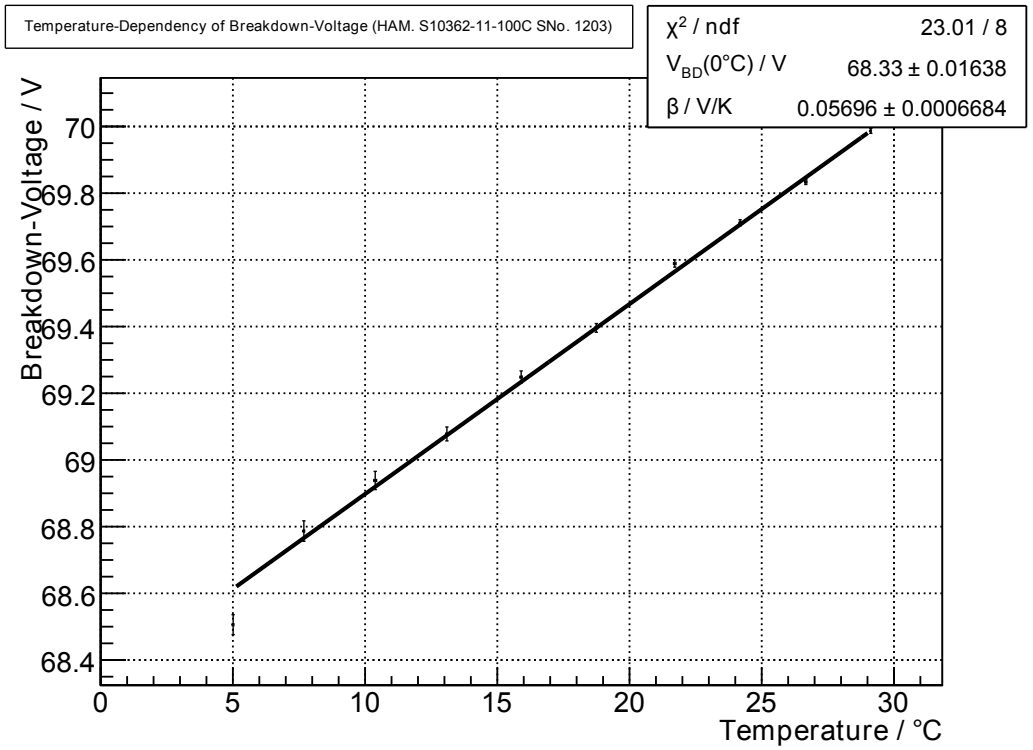

Figure 4.6: Temperature dependency of the breakdown voltage of SiPM-type Hamamatsu S103612-11-100C. Data point removed compared to figure 4.6.

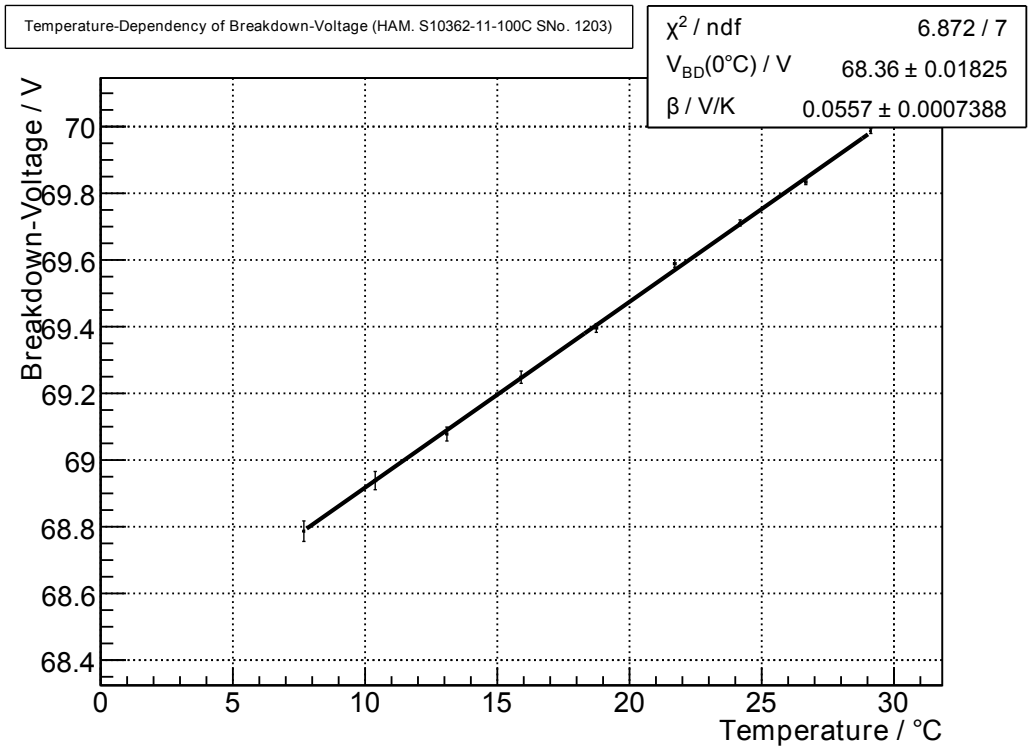

Figure 4.7: Temperature dependency of the breakdown voltage of SiPM-type Hamamatsu S103612-11-100C. Data point removed compared to figure 4.7.

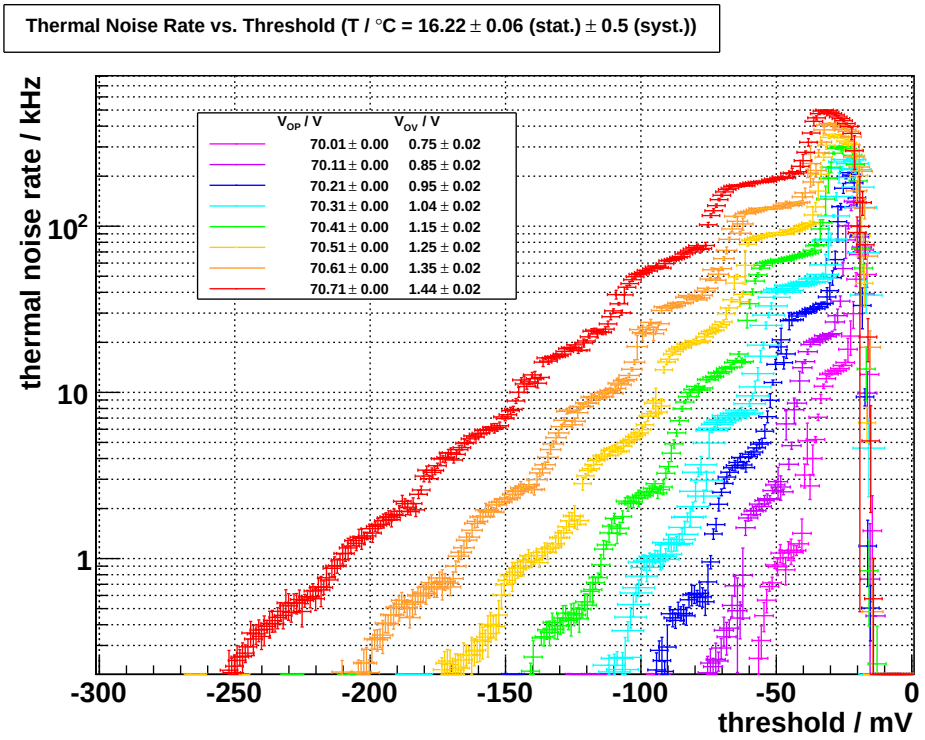

Figure 4.8: Thermal noise rate vs. threshold - various operating voltages $V_{\mathrm{OP}} = V_{\mathrm{BD}} + V_{\mathrm{OV}}$, which is equal to the sum of breakdown voltage and overvoltage.

The temperature is constant and the operating voltage is varied with $\Delta V_{\mathrm{OP}} = (100.00 \pm 10.02\,(\mathrm{syst.}))$ mV, see figure 4.8.

As expected, the signal differs with various operating voltages and therefore different overvoltages: At low overvoltages, there are fewer and fewer noise events. Additionally, the gain, which is defined as the difference between neighboring photon equivalents (p.e.) in signal height (voltage), decreases with decreasing operating voltage. The overall noise rate increases with increasing overvoltage, too. This all accords with theory in chapter 3 and miscellaneous literature, e.g. [20]. So, to compare the thermal noise rate for several temperatures, the overvoltage has to be kept constant.

4.2.4 Third Run

β^{pol2} is used to determine the breakdown voltage for any temperature, according to equation (4.3). This information allows to compare the noise rate at given temperatures without the effect of *overvoltage* described before.

Figure 4.9 shows the result for a fixed overvoltage $V_{\mathrm{OV}} = (1.37 \pm 0.03)$ V. It is obvious, that the differences between trigger rates are equal for equivalent temperature differences (note: logarithmic noise scale). Solitary exception is the 19.19 °C curve; that is because of a slightly different overvoltage of 1.34 V compared to the others. In addition the temperature differences are not even. They vary between 4.96 °C and 5.81 °C.

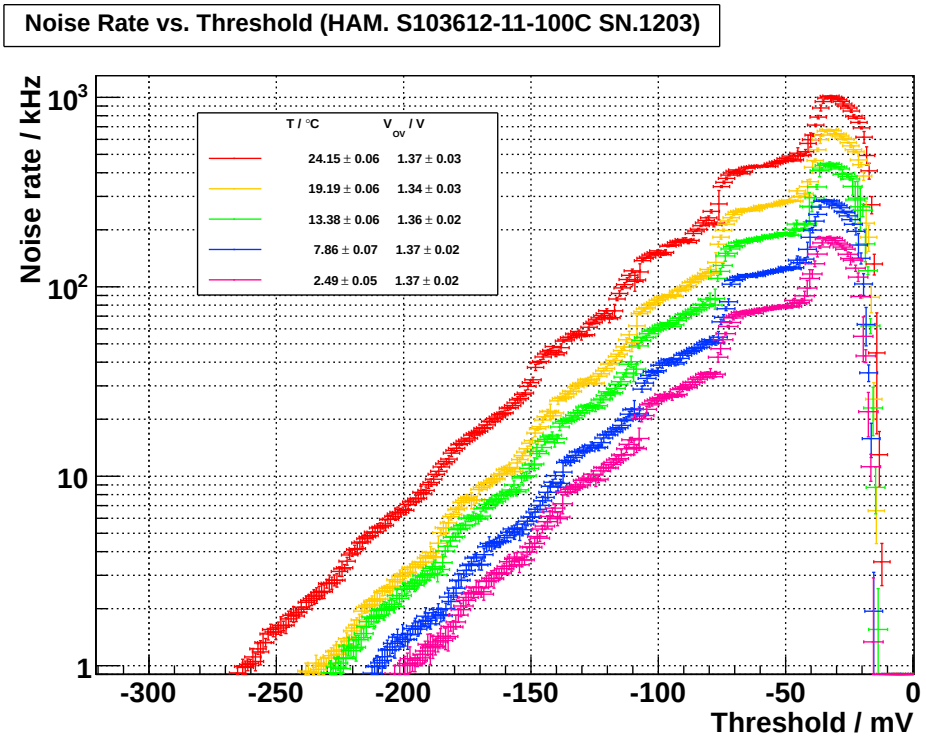

Figure 4.9: Thermal noise rate vs. threshold for various temperatures T and constant overvoltage V_{OV}.

The gain is nearly the same for a given overvoltage and various temperatures. So, the gain does not depend explicitly on the temperature rather than on the overvoltage, which is linearly temperature dependent itself.

Figure 4.10 shows the thermal noise rates versus threshold for a further series of measurements. They all show the characteristics discussed above. The noise rate now decreases with decreasing temperature, which meets the expectation discussed earlier.

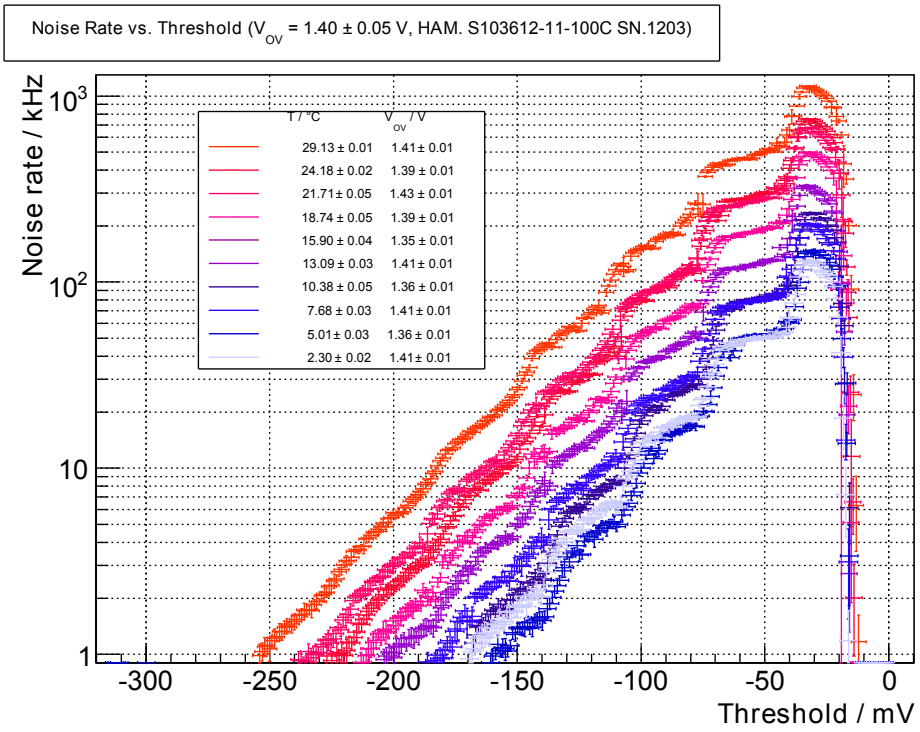

Figure 4.10: Thermal noise rate vs. threshold for various temperatures T and nearly constant overvoltage V_{OV}.

5. Relative Photon Detection Efficiency

Like any object, silicon photomultipliers experience light reflection effects. In this chapter the relative photon detection efficiency with respect to the incident angle of light is studied.

Silicon photomultipliers consist of an insensitive area hosting quenching resistors that lie right around the sensitive part. If SiPMs are combined to a light detector array, it will be desirable to reduce this insensitive part by using light focus devices, like light funnels (e.g. Winston cones) or micro-lens arrays. Therefore, initially vertical incident photons can change their angle of impact on the SiPM due to reflections on the surface of the funnel or by lensing effects, respectively.

To concede a usage of these light focus devices, it is necessary that the overall detection efficiency will not suffer.

This chapter addicts on the relative photon detection efficiency depending on the incident angle of light. To focus the light Winston cones are considered.

5.1 Experimental Setup

It is very important to follow certain steps to realize a controlled environment. A dark box, for instance, is used to distract all light sources from penetrating the experimental setup. A LED is used as a light source, which is pulsed by a HP pulse generator, cf. chapter 3. As we wish to measure data for different angles of incidence for this light bulb, the silicon photomultiplier and its frontend board are placed on a rotary disc (these three are called *SiPM-system* in further context). To ensure data acquisition correctly cables for power sources and electronics are lead through connectors in the dark box.

The light source was diffused by using an integrating sphere, and parallelized by using a pinhole aperture and a confocal lens (*geometric-optical-system*). As the light still propagates within a solid angle, its spread was measured beforehand:

$$\begin{aligned} \theta_{\text{inc}} &= \arctan \frac{d_2 - d_1}{2\,L} \\ &\approx (0.06 \pm 0.01)\,^\circ, \end{aligned} \tag{5.1}$$

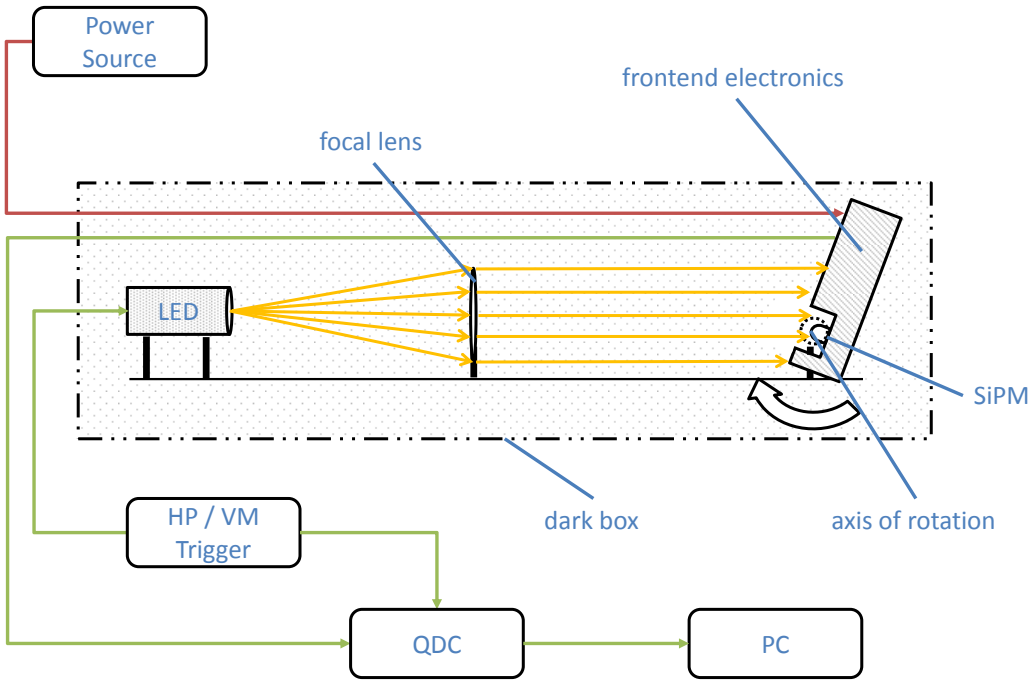

Figure 5.1: Schematic view of the relative Photon Detection Efficiency (PDE) measurement setup.

where d_1 and d_2 are the diameters at the source of the ray and after the distance L. Since the edge of the light is gloomy, the uncertainty of the increasing angle θ_{inc} is rather large. However, this spread is much smaller than the estimated uncertainty on the angle measurement, see the following sections for more details.

5.1.1 Setup and Timing

A schematic view of this setup is printed in figure 5.1. All parts, that are used to detect or produce light, are placed in the dark box. The *SiPM-system*, the LED and the *geometric-optical-system* are mounted at three points of a track. The cables for data acquisition and power source, like the power supplies for the frontend electronics ($\pm 5\,\mathrm{V}$), the SiPM itself ($V_{op} \sim 70\,\mathrm{V}$) and the LED ($\sim 4.6\,\mathrm{V}$) lead outside the dark-box. Two further plugs are needed for data output. At first, the SiPM output signal is connected with the Charge-Counting-Device (QDC) in one of its input channels. Secondly, as the LED is triggered remotely (HP Pulser), its signal is given to the gate channel of the QDC, so that data is taken while the LED is being flashed only.

To provide synchronous analysis, the timing has to be exactly the same for each signal. This is performed by using delay switches, which reduce the delay skewness to 0.5 ns. It can be observed and checked at an oscilloscope.

5.1.2 Data Acquisition

The QDC is now connected to a Personal Computer (PC) via the data-acquisition-frontend (VM-USB). A program has been written to acquire the output-signals of the QDC. These signals have been saved to hard disk as ROOT histograms in binary

Device	Setting	Value
Keithley 2400	V_{OP}	71.0 V
Lambda ZUP-10-20	V_{DC}	±5.0 V
VM-USB-Pulser	f	10 kHz
	T_{FWHM}	50 ns
HP-Pulser	V_{OFF}	-1.0 V
	V_{SS}	-4.6 V
	T_{FWHM}	8.0 ns
Gate Pulse	T_{FWHM}	$\sim$ 11.0 ns
	V_{P}	-700 mV

Table 5.1: Measurement dependent settings of devices used in measurement: Relative PDE

coding. These files contain two histograms, representing the same data in different resolutions and range; High and Low Gain Channel, cf. chapter 3. The data-taking-rate provided by the QDC is about 800 Hz. Assuming the SiPM event rate is higher than 1 kHz, the estimated amount of data will be $\sim 800\,\mathrm{Hz} \times 2\,\mathrm{min} = 96000$ and $\sim 800\,\mathrm{Hz} \times 1\,\mathrm{min} = 48000$ events in each histogram, respectively.

Every time the *SiPM system* has been rotated 4°, another run has been performed by the C++ program. To estimate the dark-rate, the LED is turned off and the data is taken for another 1 and 2 minutes, respectively. This measurement has been repeated four times to evaluate the statistical fluctuations of the noise and therefore the statistical error.

The measurement-dependent settings of the specified devices are shown in table 5.1. Note: The maximal angle of incidence of the emitted light is varied up to 100° to check for reflections within the dark-box. At this point one may note, that no reflections have been observed. The 100° data correspond to the *LED off* measurements pretty well, see next section.

5.2 Analysis

The easiest way to determine the relative photon detection efficiency is the measurement of the amount of light that is detected by the silicon photomultiplier for certain angles of incidence. After that, the results can be plotted, relative to an angle of incidence of 0°.

Specifically, the mean of the detected photons of the QDC spectra can be determined and compared for different incident angle of light.

However, this method is not used here, because random induced photon events, like crosstalk and afterpulses, lead to higher values than the *real* amount of detected photons, see chapter 3. To avoid the noise events, another method is implemented. The Poissonian mean is used, which can be determined from the pedestal data. These

data represent events where no avalanche process has been taken place, thereby false events (crosstalk and afterpulses) can be avoided.

Since the pulsed LED produces light with a known rate and independently of the time, the probability can be described by applying the Poisson distribution. The way this is done is described further on.

5.2.1 Used Theoretical foundations

The probability to detect N photons within a sufficiently small time interval Δt may be derived from the Poisson distribution;

$$P(N) = \frac{\lambda^N \exp -\lambda}{N!}, \tag{5.2}$$

This leads to the expected number of occurrences

$$\lambda = -\ln P(0), \tag{5.3}$$

where $P(0) = N_{PED}/N_{TOT}$ is the probability, that no photon is detected and is equivalent to the fraction of number of entries within the pedestal to all events. Hence the dark rate erroneously improves the photon detection efficiency, a correction term is needed. This results in:

$$\lambda = -\ln \frac{N_{PED}}{N_{TOT}} \cdot \frac{N_{TOT}^{DARK}}{N_{PED}^{DARK}} = \ln \frac{N_{TOT}}{N_{PED}} - \underbrace{\ln \underbrace{\frac{N_{TOT}^{DARK}}{N_{PED}^{DARK}}}_{\geq 1}}_{\geq 0} \tag{5.4}$$

N_{PED}^{DARK} and N_{TOT}^{DARK} are measured with the LED turned off. The corresponding errors of the count of events ΔN_{TOT}, ΔN_{PED}, ΔN_{TOT}^{DARK} and ΔN_{PED}^{DARK} are in first approximation the Poissonian error. This leads to the error of the expected number of occurrences

$$\Delta\lambda = \sqrt{\left(\frac{\Delta N_{TOT}}{N_{TOT}}\right)^2 + \left(\frac{\Delta N_{PED}}{N_{PED}}\right)^2 + \left(\frac{\Delta N_{TOT}^{DARK}}{N_{TOT}^{DARK}}\right)^2 + \left(\frac{\Delta N_{PED}^{DARK}}{N_{PED}^{DARK}}\right)^2}. \tag{5.5}$$

The relative Photon Detection Efficiency PDE(θ) is derived from the Poissonian λ relative to its vertical value (0°) and normalized for its loss of effective area ($\cos\theta$).

$$\mathrm{PDE}(\theta) = \frac{\lambda(\theta)}{\lambda(0^\circ)} \cdot \frac{1}{\cos(\theta)} \tag{5.6}$$

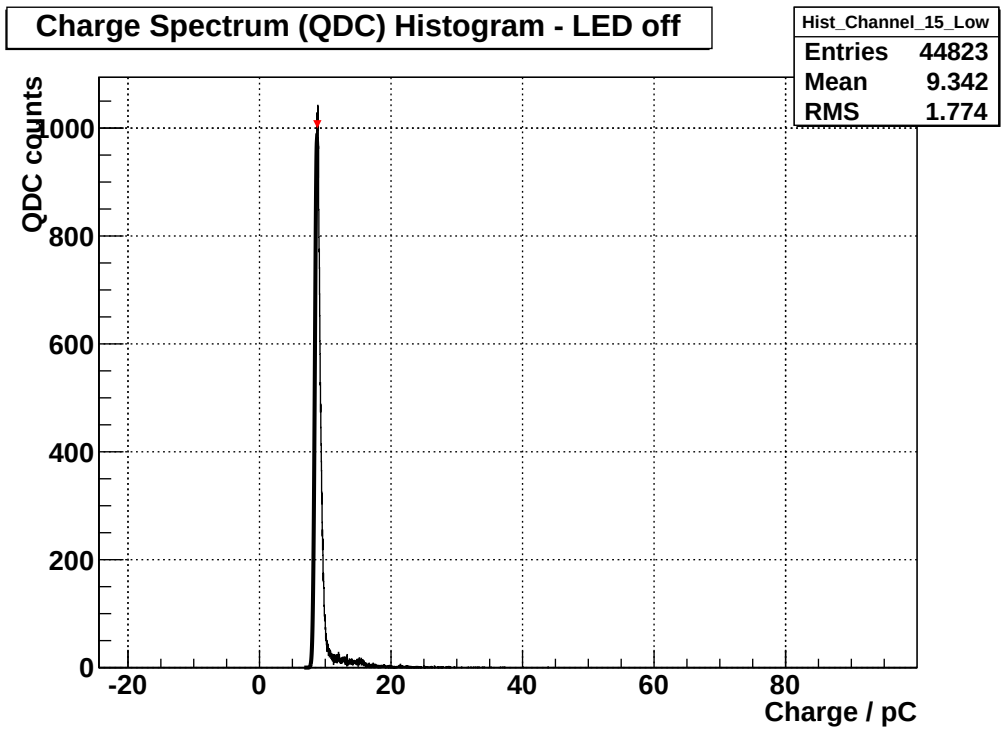

Figure 5.2: QDC spectrum of amplified silicon photomultiplier output signal. LED is turned off. The pedestal peak is clearly visible.

Its error is

$$\Delta\mathrm{PDE}(\theta) = |\mathrm{PDE}(\theta)| \cdot \sqrt{\left(\frac{\Delta\lambda(\theta)}{\lambda(\theta)}\right)^2 + \left(\frac{\Delta\lambda(0°)}{\lambda(0°)}\right)^2 + (\Delta\theta \cdot \tan\theta)^2} \tag{5.7}$$

(Note the absolute value of the PDE as it may become negative mathematically; although the measurements shall be compatible with greater or equal 0 within their errors). Since the measuring of θ was done by hand, its error is needed to be estimated as $\Delta\theta = 1°$, confer with the spread of the beam in equation (5.1) on page 27.

5.2.2 First Data Analysis

To find the individual photon-equivalent (p.e.) peaks of the output spectrum of the QDC (fig. 5.2) programmatically, the ROOT class *TSpectrum* has been implemented. This functionality returns the peaks greater a specific threshold, which can be varied by the user himself. As it can be seen from figure 5.2, the largest peak found will be the pedestal equivalence when the LED is turned off.

Since statistical fluctuations around the mean of the pedestal are normal distributed, a Gaussian fit has been made, see figure 5.3. The $\chi^2 \,/\, \mathrm{ndf} \approx 20.03$ of this fit is rather large. After a close look at the QDC-distributed data, it seems that the individual

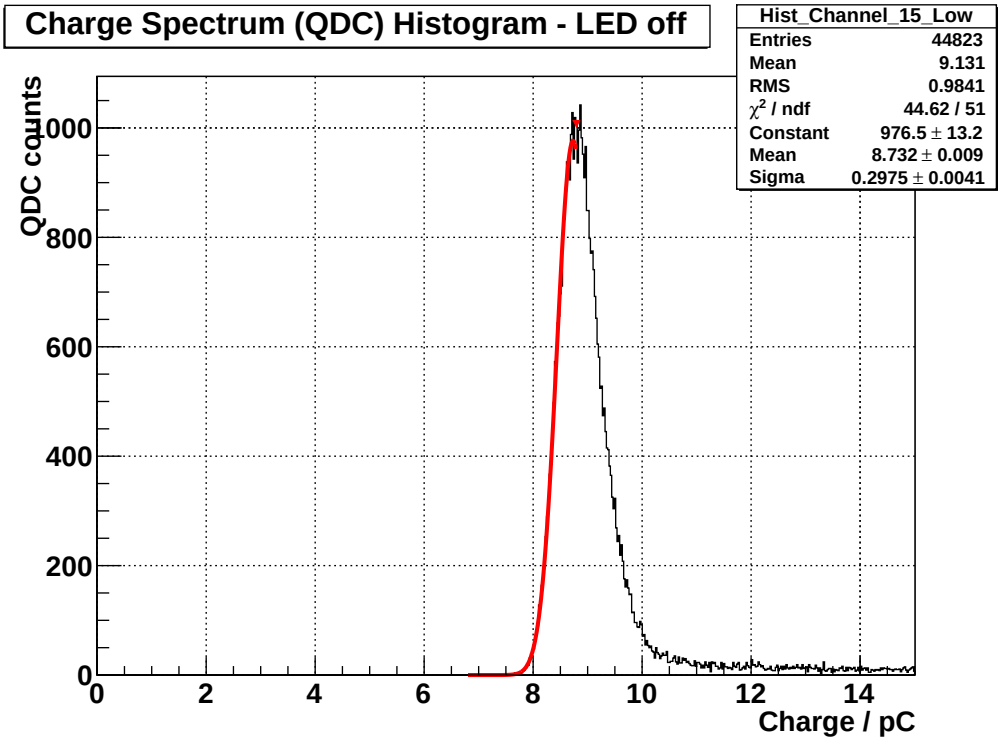

Figure 5.3: QDC spectrum of amplified silicon photomultiplier output signal. LED is turned off. Gaussian fit (red) applied on the left side of the pedestal peak.

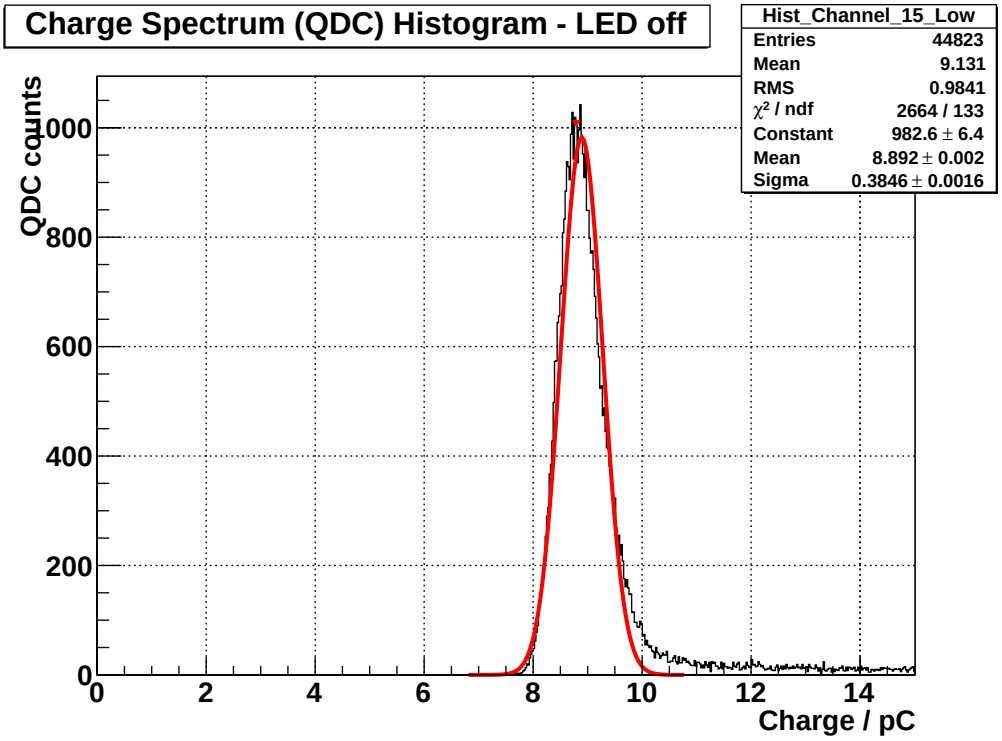

Figure 5.4: QDC spectrum of amplified silicon photomultiplier output signal. LED is turned off. Gaussian fit (red) applied on the pedestal peak, showing skewness of pedestal peak.

peaks are slanted. It is called *skewness of a function*. However, each side of this peak is normal distributed, as it can be seen in figure 5.4.

The theoretical current I_0 that has been *generated* by a zero-photon event (which means, that no photon has been detected) is equal to the leakage current I_{leak}. This is the minimal possible current (cf. chapter 3). Statistical fluctuations lead to a normal distribution on the left side of this peak.

Plotting the current I versus time t, the area beneath the curve is equal to the charge $Q = \left|\int I \, \mathrm{d}t\right|$. The charge retrieved by this area is always positive; so, the right side of the peak follows two Gaussian distributions. Additionally, a *negative* charge cannot be generated. This is the reason why these peaks are left-slanted (and have more events, greater than their mean).

To avoid this problem, one can apply a background analysis of these histograms and add a multi-Gaussian-fit. Another method is an estimation of the range of the pedestal by hand, which has been used in this bachelor-thesis.

This yields

$$\Delta^P N_{TOT}^{DARK} = \sqrt{N_{TOT}^{DARK}} \qquad \Delta^P N_{TOT}^{PED} = \sqrt{N_{TOT}^{PED}}, \tag{5.8}$$

where $\Delta^P N_{TOT/PED}^{DARK}$ are the Poissonian errors on $N_{TOT/PED}^{DARK}$. Because statistical fluctuations $\Delta^S N$ are rather small, compared to $\Delta^P N$, these errors can be neglected. The expected amount of dark count events is given by

$$\lambda^{\mathrm{DARK}} = \frac{N_{TOT}^{DARK}}{N_{PED}^{DARK}}. \tag{5.9}$$

Error propagation leads to

$$\begin{aligned} \Delta\lambda^{\mathrm{DARK}} &= \sqrt{\left(\frac{\Delta N_{TOT}^{DARK}}{N_{TOT}^{DARK}}\right)^2 + \left(\frac{\Delta N_{PED}^{DARK}}{N_{PED}^{DARK}}\right)^2} \\ &\approx \sqrt{\frac{1}{N_{TOT}^{DARK}} + \frac{1}{N_{PED}^{DARK}}}. \end{aligned} \tag{5.10}$$

The same procedure is done with the LED turned on, for different angles of incidence θ. Figure 5.5 shows the output spectrum of the QDC for $\theta = 0°$. It is clearly visible, that more photons have been detected here, than for the LED turned off.

For direct comparison, plots for $\theta = 40°$ and $\theta = 92°$ are shown in figures 5.6 and 5.7. For $\theta = 0°$ the 7^{th} photon equivalent peak can be seen, beside the first one, which is known as the pedestal. In the $\theta = 40°$ and $\theta = 92°$ plots, only the 5^{th} photon equivalent and the pedestal peak are visible, respectively. This means, that a lesser amount of photons have been detected here.

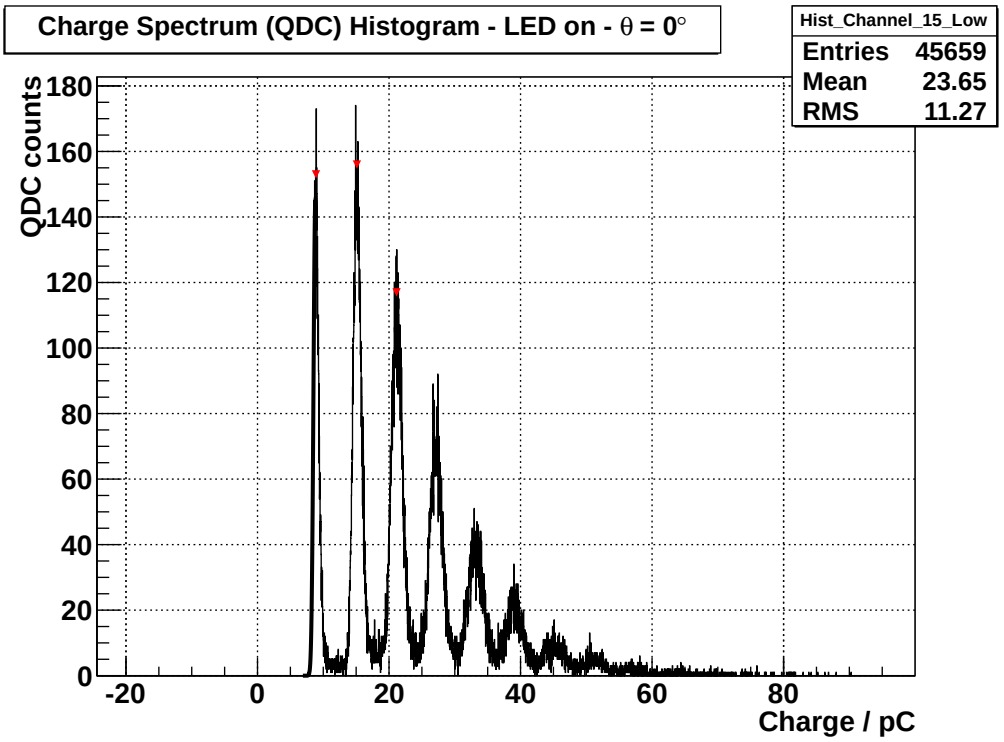

Figure 5.5: QDC spectrum of amplified silicon photomultiplier output signal. LED is turned on. Incident angle of light $\theta = 0°$.

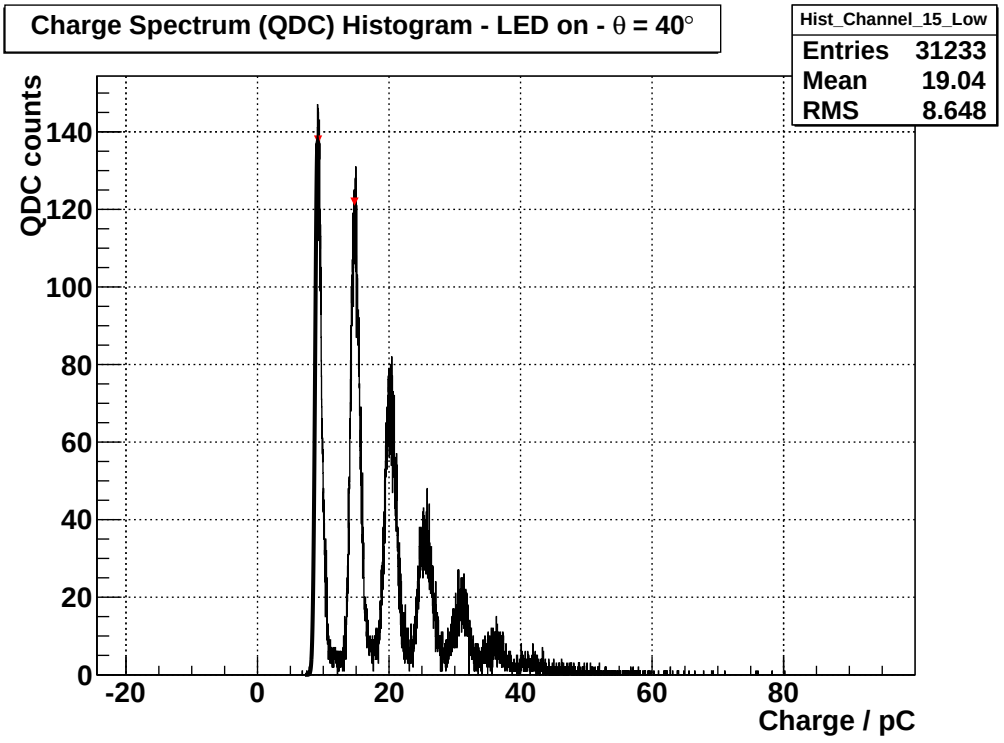

Figure 5.6: QDC spectrum of amplified silicon photomultiplier output signal. LED is turned on. Incident angle of light $\theta = 40°$.

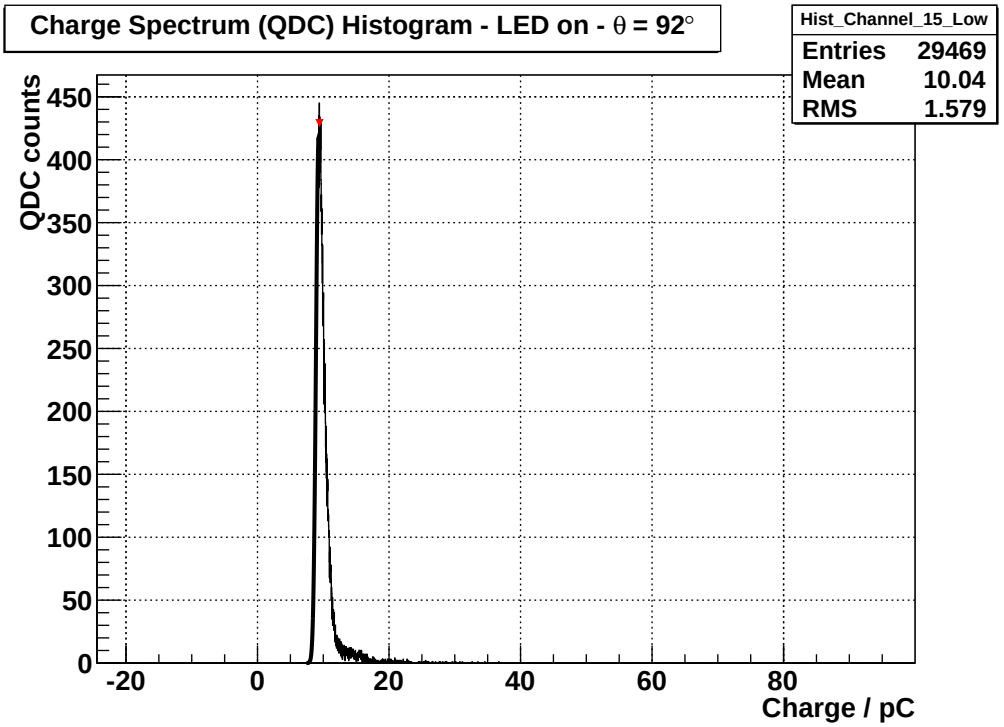

Figure 5.7: QDC spectrum of amplified silicon photomultiplier output signal. LED is turned on. Incident angle of light $\theta = 92°$.

The dependency of the relative photon detection efficiency versus the incident angle of light is printed in figure 5.8. The relative photon detection efficiency is quite stable from 4° to 32°, but drops beneath 90% at an angle of incidence greater 60° and equal. At $\theta \geq 72°$, the relative PDE suddenly breaks in. This has to be verified by comparing the data with theory.

5.2.3 Theory and Experiment

Whenever light travels from one medium with refractive index n_1 to another with refractive index n_2, there is a chance of reflection and transmittance (also known as refraction). The reflection coefficients of perpendicular polarized light $R_\perp$ and parallel polarized light $R_\parallel$ are given by [22]

$$R_\perp(\theta, \eta) = \left(\frac{n_1 \cos\theta - n_2 \cos\eta}{n_1 \cos\theta + n_2 \cos\eta}\right)^2 \qquad R_\parallel(\theta, \eta) = \left(\frac{n_1 \cos\eta - n_2 \cos\theta}{n_1 \cos\eta + n_2 \cos\theta}\right)^2, \quad (5.11)$$

where θ is the angle of incidence of light. This can be expressed without the transmitted angular η, by applying Snell's law

$$n_1 \sin\theta = n_2 \sin\eta \qquad \Rightarrow \cos\eta = \sqrt{1 - \left(\frac{n_1}{n_2} \sin\theta\right)^2}. \quad (5.12)$$

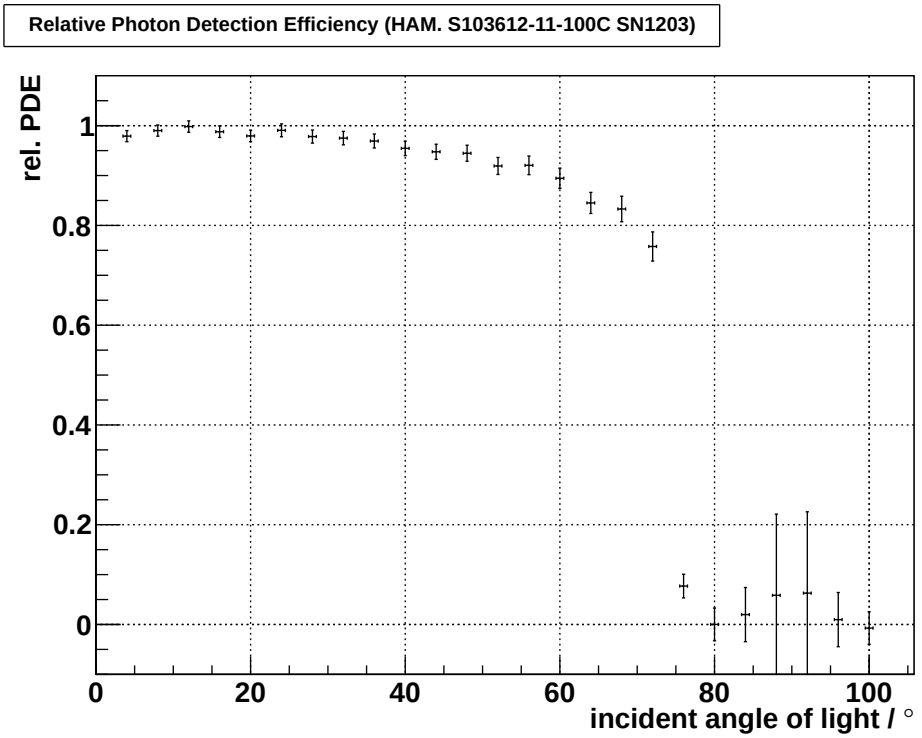

Figure 5.8: Relative photon detection efficiency as a function of the incident angle of light.

Unpolarized light can be approximated as

$$\begin{aligned} \mathrm{R}(\theta) &= \frac{\mathrm{R}_{\perp} + \mathrm{R}_{\parallel}}{2} \\ &= \frac{1}{2}\left\{\left(\frac{n_1\cos\theta - n_2\cos\eta}{n_1\cos\theta + n_2\cos\eta}\right)^2 + \left(\frac{n_1\cos\eta - n_2\cos\theta}{n_1\cos\eta + n_2\cos\theta}\right)^2\right\}. \end{aligned} \tag{5.13}$$

The chance of transmittance/refraction is given by [23]

$$\mathrm{T}(\theta) = 1 - \mathrm{R}(\theta). \tag{5.14}$$

Compared to the experimental data in figure 5.8 on page 36, Fresnel equations expect too many photons, which are transmitted into the silicon of the SiPM (see figure 5.9). So, we have some kind of *light-leak* here, which has to be explained and analyzed. This is part of this section.

As it can be seen in figure 5.9, variations in the indices of refraction ($\Delta n_j = \pm 0.1$) will not explain the difference between the data and the expected dependency from theory. So, there has to be some other reason for this light leak for higher angles.

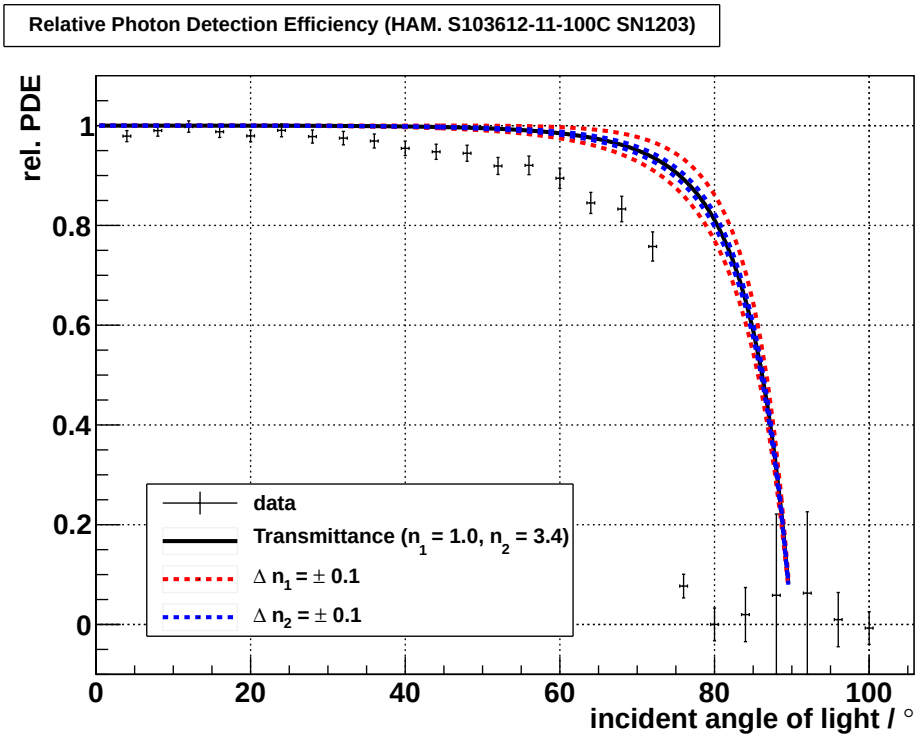

Figure 5.9: Relative photon detection efficiency with Fresnel equation. Red- and blue-dotted lines show variations in $n_1 = 1.0$ and $n_2 = 3.4$ of $\Delta n_j = \pm 0.1$.

5.2.4 Additional coating

The manufacturer of the SiPM, tested in this environment, has stated in private communication, that their products are coated with a silicon resin. This oxide has a similar refraction index to SiO_2, $n_{\text{resin}} = n_2 \approx 1.4$, which is known to be used in production of silicon photomultipliers [5]. The coating reduces the amount of reflected photons (see chapter 3). Hamamatsu approached this value, so an uncertainty of $\Delta n_{\text{resin}} = \pm 0.05$ is used further on, since the unrounded refractive index can be between 1.35 and 1.44.

This affects the analysis. Fresnel equations become more complicated, because the count of boundary layers increases from 1 to 2. We have to factor in additional reflections within the second layer. The schematics can be found in figure 5.10.

The first order approximation of the transmittance $\mathrm{T}^{1^{st}}$ for two-layer refraction is derived from Fresnel's equations. The possibility of a photon to be transmitted from n_1 to n_2 $\mathrm{T}^{n_2}_{n_1}$ and again from n_2 to n_3 ${}^{n_3}_{n_2}\mathrm{T}$ is just the product of each transmittance. Thus it becomes

$$\mathrm{T}^1(\theta, \eta) = {}^{n_2}_{n_1}\mathrm{T}(\theta) \cdot {}^{n_3}_{n_2}\mathrm{T}(\eta), \tag{5.15}$$

where θ is the incident angle of light in n_1, and η is the angle of the transmitted photon. We can see from figure 5.10 on page 38, that the angle within n_2 does

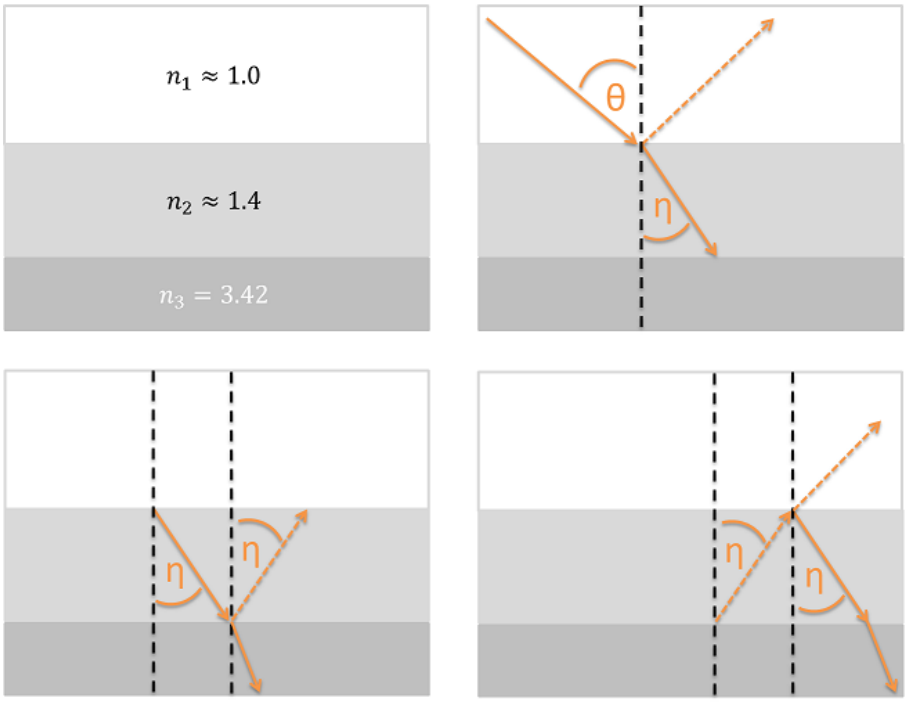

Figure 5.10: Schematics of multiple reflection layers within a silicon photomultiplier. Values of refractive indices are given for Hamamatsu S103612-11-100C

not change, but depends on θ and is equal to η. The transmittance in first order approximation is normalized with its value for $\theta = 0° \rightarrow \eta = 0°$. This leads to

$$\mathrm{T}^{1^{\mathrm{st}}}(\theta,\eta) = \frac{\mathrm{T}^1(\theta,\eta)}{\mathrm{T}^1(0°,0°)} = \frac{{}^{n_2}_{n_1}\mathrm{T}(\theta)\cdot{}^{n_3}_{n_2}\mathrm{T}(\eta)}{{}^{n_2}_{n_1}\mathrm{T}(0°)\cdot{}^{n_3}_{n_2}\mathrm{T}(0°)}. \tag{5.16}$$

$T^{2^{\mathrm{nd}}}$ includes $T^{1^{\mathrm{st}}}$ and the second order approximation. It is given by

$$\begin{aligned}\mathrm{T}^{2^{\mathrm{nd}}}(\theta,\eta) &= \frac{\mathrm{T}^1(\theta,\eta)+\mathrm{T}^2(\theta,\eta)}{\mathrm{T}^1(0°,0°)+\mathrm{T}^2(0°,0°)} \\ &= \frac{{}^{n_2}_{n_1}\mathrm{T}(\theta)\cdot{}^{n_3}_{n_2}\mathrm{T}(\eta) + {}^{n_2}_{n_1}\mathrm{T}(\theta)\cdot{}^{n_3}_{n_2}\mathrm{R}(\eta)\cdot{}^{n_1}_{n_2}\mathrm{R}(\eta)\cdot{}^{n_3}_{n_2}\mathrm{T}(\eta)}{{}^{n_2}_{n_1}\mathrm{T}(0°)\cdot{}^{n_3}_{n_2}\mathrm{T}(0°) + {}^{n_2}_{n_1}\mathrm{T}(0°)\cdot{}^{n_3}_{n_2}\mathrm{R}(0°)\cdot{}^{n_1}_{n_2}\mathrm{R}(0°)\cdot{}^{n_3}_{n_2}\mathrm{T}(0°)}.\end{aligned} \tag{5.17}$$

${}^{n_3}_{n_2}\mathrm{R}(\eta)$ and ${}^{n_1}_{n_2}\mathrm{R}(\eta)$ are the probabilities for reflection between the media n_2 to n_3 and n_2 to n_1, respectively. For small angles $\alpha \leq 50°$ the first-order approximation fits very well the experimental data, since the transmittance between the resin (n_2) and the silicon (n_3) is quite high.

To see what happens at higher orders, one can evaluate the j^{th}-order approximation as

$$T^{j^{\mathrm{th}}}(\theta,\eta) = \frac{{}^{n_2}_{n_1}\mathrm{T}(\theta)\cdot{}^{n_3}_{n_2}\mathrm{T}(\eta)\cdot\sum_{k=0}^{j-1}\left({}^{n_1}_{n_2}\mathrm{R}(\eta)\cdot{}^{n_3}_{n_2}\mathrm{R}(\eta)\right)^k}{{}^{n_2}_{n_1}\mathrm{T}(0°)\cdot{}^{n_3}_{n_2}\mathrm{T}(0°)\cdot\sum_{k=0}^{j-1}\left({}^{n_1}_{n_2}\mathrm{R}(0°)\cdot{}^{n_3}_{n_2}\mathrm{R}(0°)\right)^k}. \tag{5.18}$$

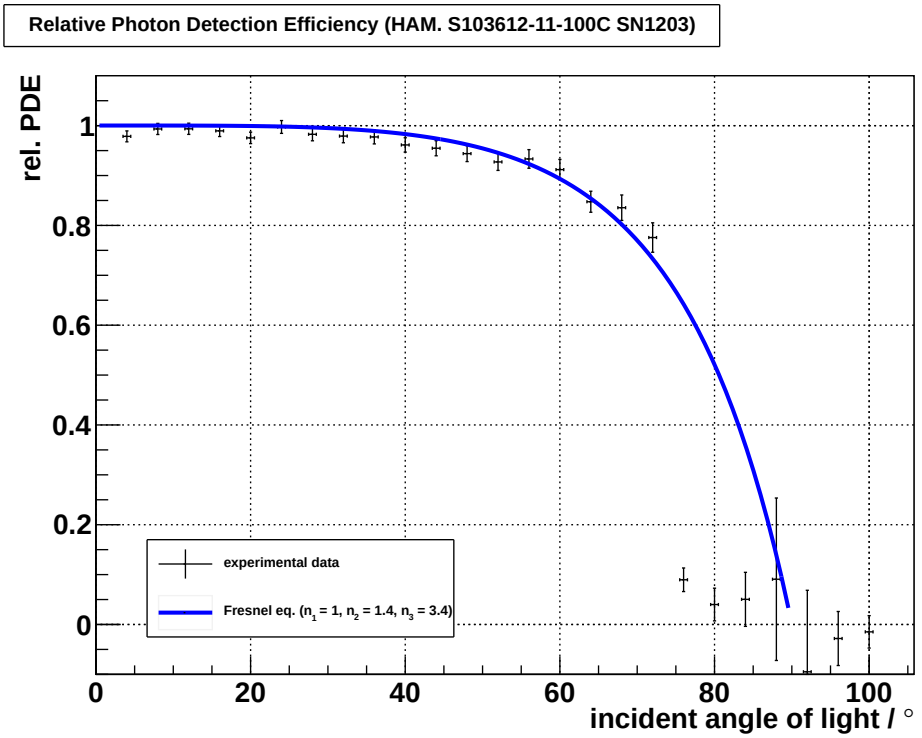

Figure 5.11: Relative Photon Detection Efficiency with Fresnel equation derived in equation (5.19) (no approximation).

For j $\to \infty$, equation (5.18) becomes

$$\boxed{T^{\infty^{\text{th}}}(\theta,\eta) = T(\theta,\eta) = \frac{{}^{n_2}_{n_1}\mathrm{T}(\theta)\cdot {}^{n_3}_{n_2}\mathrm{T}(\eta)\cdot\left(1-{}^{n_1}_{n_2}\mathrm{R}(0°)\cdot {}^{n_3}_{n_2}\mathrm{R}(0°)\right)}{{}^{n_2}_{n_1}\mathrm{T}(0°)\cdot \mathrm{T}^{n_3}_{n_2}(0°)\cdot\left(1-{}^{n_1}_{n_2}\mathrm{R}(\eta)\cdot {}^{n_3}_{n_2}\mathrm{R}(\eta)\right)}.} \tag{5.19}$$

The geometric progression has been used here:

$$\sum_{k=0}^{\infty} a^k = \frac{1}{1-a}, \text{ with } a < 1. \tag{5.20}$$

Equation (5.19) can be evaluated from $\theta = 0° \ldots 90°$, as shown in figure 5.11. This represents the *real* transmitted amount of photons. The theory now fits well with the experimental data, but we still have some point missed out, since the fit does not match data for angles $\theta \geq 76°$. This can be explained by certain problems with the experimental setup that have occurred during measurement. This is part of the next section.

5.2.5 Frontend Barrier

The silicon photomultiplier is embedded within the Frontend electronics and sleaze to absorb any reflected light, shown in figure 3.8 on page 13. If this board is being

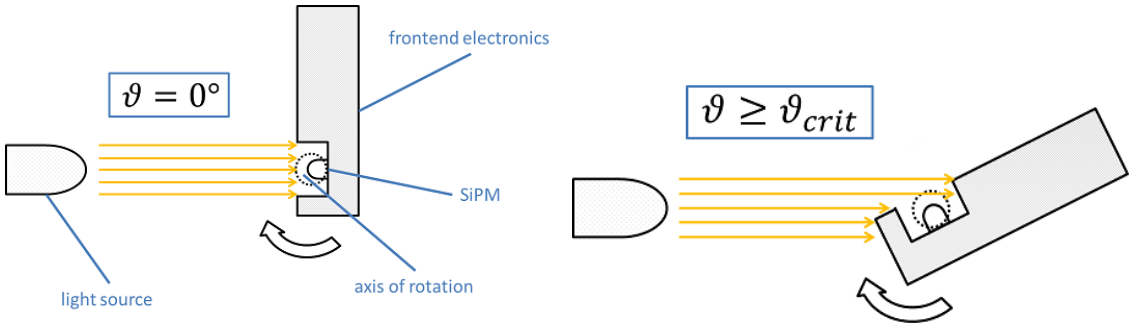

Figure 5.12: Frontend electronics and SiPM pattern seen from above. Compare with figure 3.8

turned around its axis of rotation, the SiPM may move into the blind angle of the LED. Schematics of this phenomenon are shown in figure 5.12.

The critical angle θ_{crit} at which the SiPM will not be hit by light anymore can be derived by figure 5.13 on page 41 as

$$\theta_{\text{crit}} = \arctan \frac{b}{a}, \tag{5.21}$$

where a is the *deepness* of the SiPM within the electronics and b is the distance between the SiPM sensitive area and the edge of the board, with respect to the rotation-plane. These values have been measured afterwards as

$$\begin{aligned} a &= (0.33 \pm 0.05)\ \text{mm} \\ b &= (1.44 \pm 0.05)\ \text{mm} \\ \Rightarrow \theta_{\text{crit}} &= (77.09 \pm 1.93)\ ^\circ \end{aligned} \tag{5.22}$$

This zone can be added to the plot; more specifically, the data beyond θ_{crit} may be ignored, see figure 5.14. The expected relative photon detection efficiency now really fits the experimental data.

The relative photon detection efficiency, depending on the incident angle of light, follows the Fresnel's equations, as predicted. The exact knowledge of the refractive indices is not necessary rather than the different coatings and layers on top of the silicon photomultipliers. This result can be used for simulations of systems, combining Winston cones and silicon photomultiplier, see chapter 6.

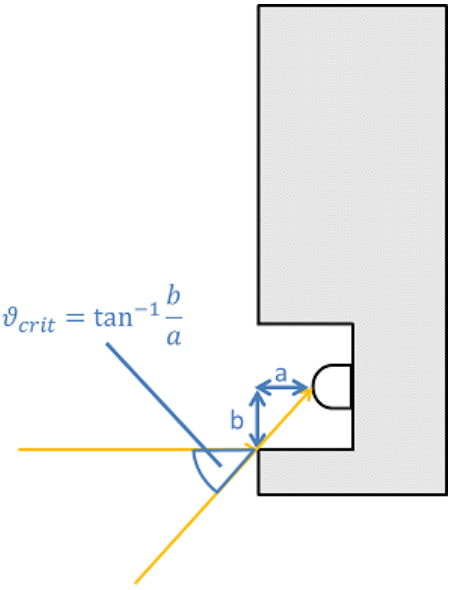

Figure 5.13: Frontend electronics and SiPM pattern seen from above. θ_{crit} is equivalent to the blind angle of the LED, cf. with text.

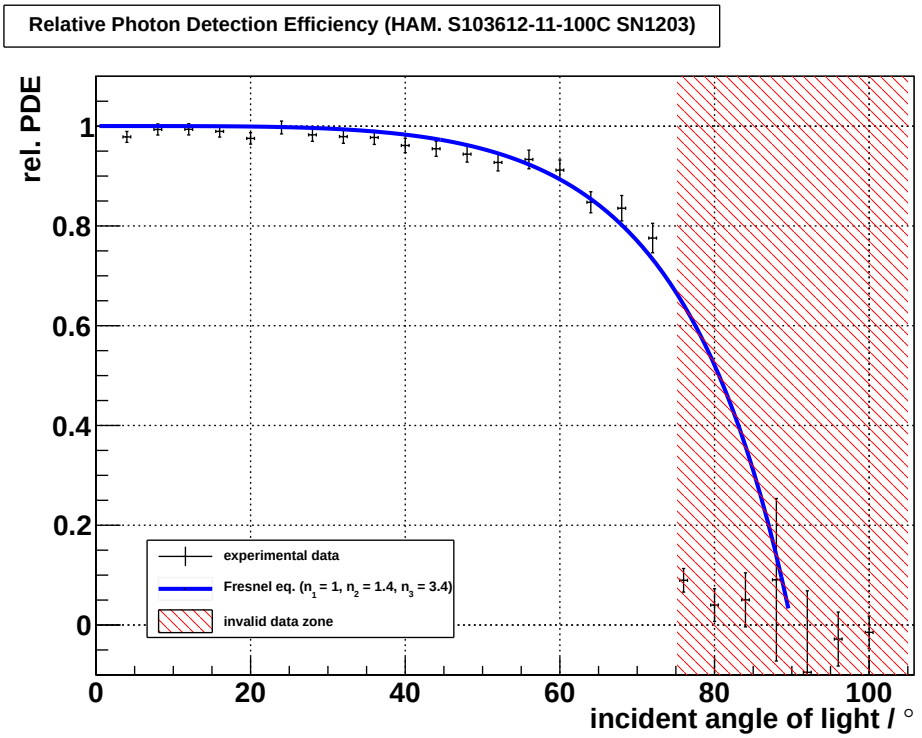

Figure 5.14: Same as figure 5.11. Dead zone (invalid data zone) added, as calculated in subsection 5.2.5.

6. System of Winston Cone and Silicon Photomultiplier

To estimate the efficiency of a system which combines Winston cones and silicon photomultipliers, a simulation is needed. These light concentrators can be used to eliminate dead space between the silicon photomultipliers to increase the detection efficiency. Due to reflections within the cone, however, the efficiency might suffer. This chapter investigates a usage of these systems.

6.1 Winston Cones

Winston cones are light funnels, which are able to focus photons from a bigger circular area with radius R_1 to a smaller area, with radius R_2, see figures 6.1 and 6.2. The most important feature is the ability, to focus light on the target surface up to a critical angle $\theta_{\max}$ with only one reflection.

Winston cones are parabolas, which have been tipped by an angle $\theta_{\max}$ and rotated on their own axis (paraboloid of revolution).

Additional mathematic subtleties are relinquished, due to no greater importance. These foundations can be comprehended from the original Winston cone publications [24].

The following properties can be read from figure 6.1: L is the length of the Winston cone and f its focal length. A common used (and important) value, is described by the compression $\alpha = R_1/R_2$, which is the ratio of the radii of the cone.

$$f = R_2 \cdot (1 + \sin\theta_{\max}) \tag{6.1}$$

$$L = \frac{R_1 + R_2}{\tan\theta_{\max}} \tag{6.2}$$

$$\sin\theta_{\max} = \frac{R_2}{R_1} = \frac{1}{\alpha} \tag{6.3}$$

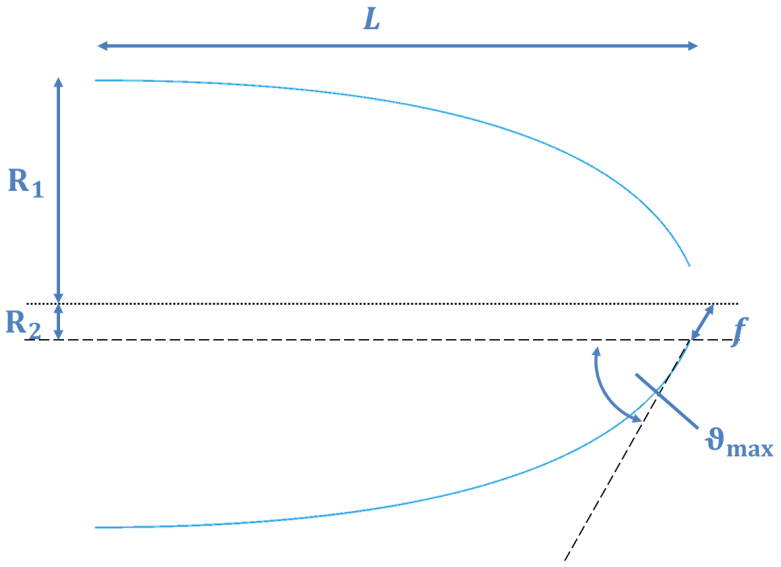

Figure 6.1: Schematic diagram of a Winston cone (light blue). Entrance R_1 and exit apertures R_1, length L, tipped angle $\theta_{\max}$ also known as opening half angle and focal length f are plotted.

6.2 Simulation of Winston Cones

6.2.1 Properties and Settings

A Monte-Carlo-simulation has been written in C++, to retrieve a first impression of the angular-distribution of the exit angle of light, after being passed through a Winston cone. Graphical simulations of a Winston cone can be seen in figure 6.6 ($\theta = 0°$) and 6.7 ($\theta = 15°$) on page 47.

The following assumptions and settings used by this simulation have been made;

- light is described as particles (photons)
- hard-scattering of photons on surface ($\theta_{\text{in}} = \theta_{\text{reflected}}$)
- several absorption coefficient ($0\% - 20\%$)
- vertical and random (up to $\theta_{\max}$) start conditions of photon angular
- photons are uniformly distributed on startup (along focal plane)
- changing in the properties of the Winston cone (radius R_1 and R_2 and therefore length L and opening angle $\theta_{\max}$)
- $10,000$ simulated photons

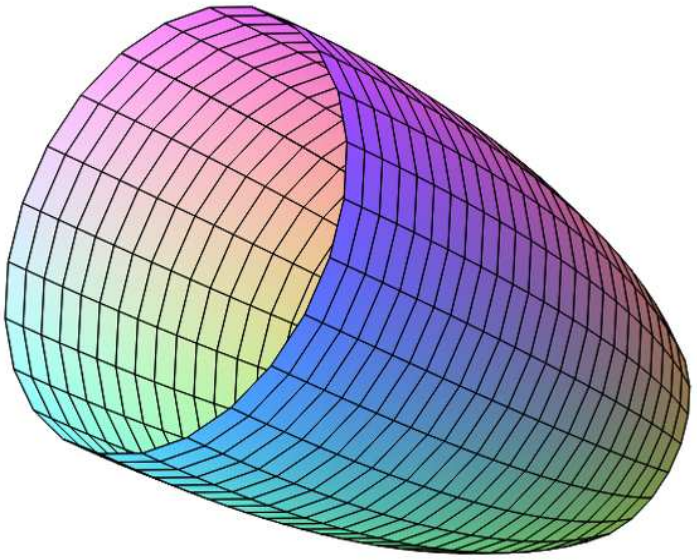

Figure 6.2: A simulated Winston cone with compression $\alpha = R_1/R_2 = 2$.

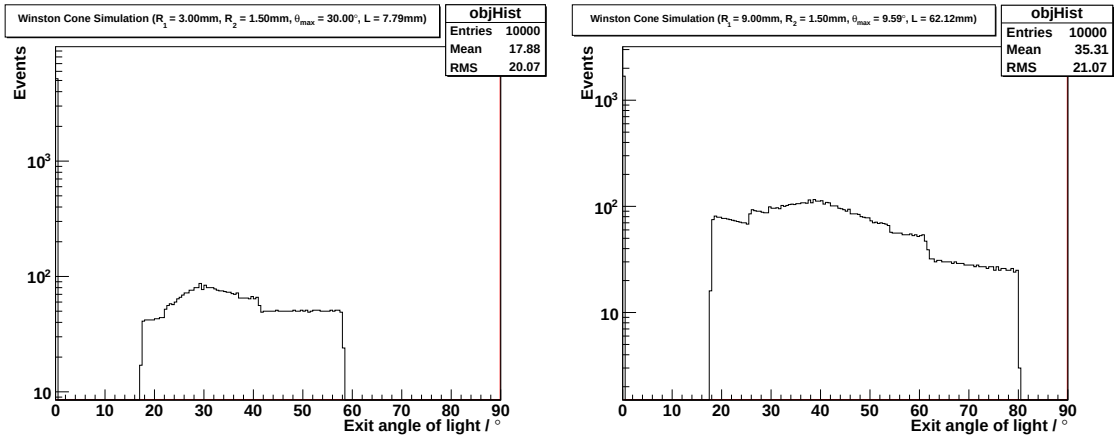

Figure 6.3: Simulated exit angles of a Winston cone with angle of incidence $\theta = 0°$ and compression $\alpha = R_1/R_2 = 2$ (left) and $\alpha = 6$ (right).

6.2.2 Simulation

The first Monte-Carlo-simulation has been done with a vertical angle of incidence ($\theta = 0°$) and no absorption ($\beta = 0\%$). The results are shown in figure 6.3, page 45 for the compression $\alpha = 2$ and $\alpha = 6$. Many photons ($\alpha = 2$: 51% and $\alpha = 6$: 17%) leave the Winston cone with an angle of $\theta = 0°$, since these particles just pass through the funnel without any interaction at all. The Winston cone is very round-shaped at the bottom near the exit, so it is not surprising, that no photon leaves the cone with an angle $\theta \in (0°, 16°)$. This, however, does not depend on α.

The distribution of $\theta \geq 16°$ effects the efficiency of the system heavily, since the amount of transmitted particles decreases with increasing angle of incidence, corresponding to Fresnel's equations (5.13), chapter 5 on page 36.

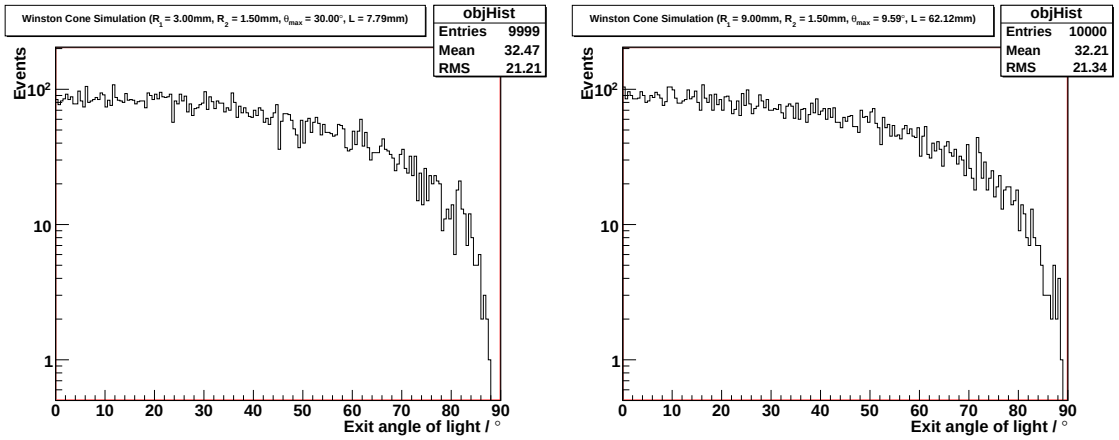

Figure 6.4: Simulated exit angles of a Winston cone with random angle of incidence $|\theta| \leq \theta_{\max}$ and compression $\alpha = R_1/R_2 = 2$ (left) and $\alpha = 6$ (right).

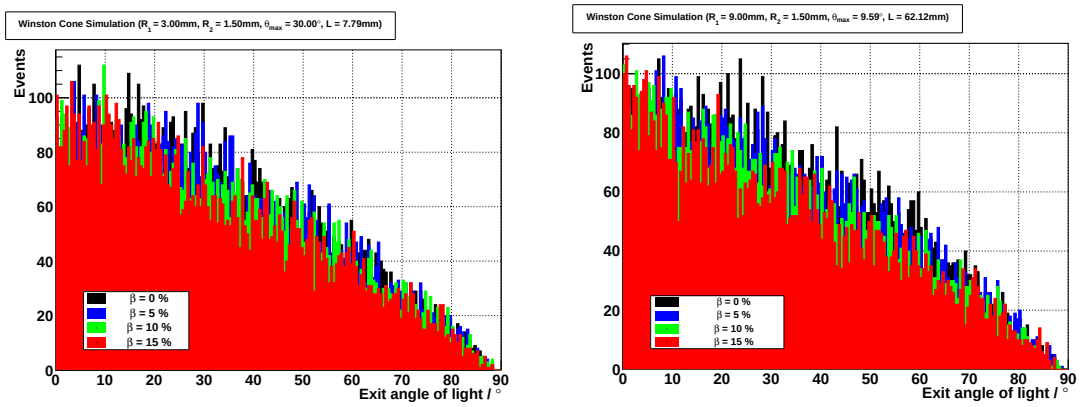

Figure 6.5: Simulated Exit angles of a Winston cone with random angle of incidence $\theta \leq \theta_{\max}$ and different absorption-coefficients β. Compression $\alpha = R_1/R_2 = 2$ (left) and $\alpha = 6$ (right).

The shape of the histogram changes, when a random angle of incidence is used instead of a vertical intrusion (seen in figure 6.4). The alteration in compression α are not as strong as for a constant angle. Most noticeable change is the fact, that no zone in θ exists, where no photons exit the cone, compared to $\theta = 0°$. Also more photons leave the funnel, with an exit-angle greater 80°. This, however, reflects the reality quite well, since photons will not penetrate the cone uniformly with a constant angle of $\theta = 0°$. Last but not least, plots with absorptions can be seen in figure 6.5. A higher compression ratio α leads to a θ-distribution with a bigger mean-value, since less photons exit the cone without any interaction at all.

6.2.3 Convolution - System of a Winston Cone and a Silicon Photomultiplier

What we are really interested in, is the overall efficiency for a system that combines a Winston cone and a silicon photomultiplier. Therefore, the results from section 5.2 and 6.2 are convoluted.

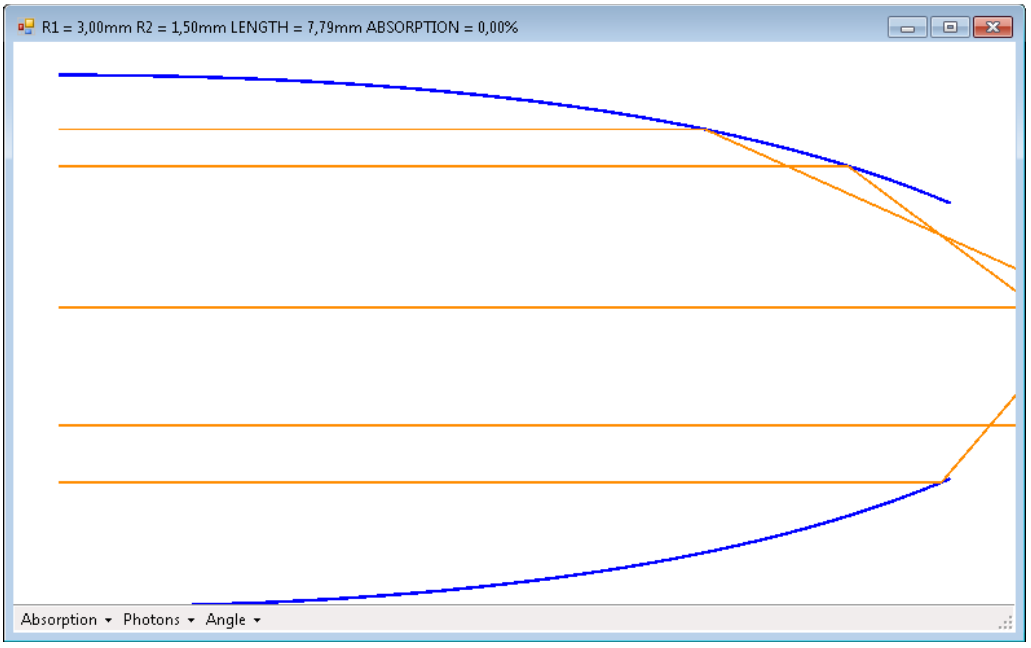

Figure 6.6: Graphical Implementation (Windows 7 C# .NET) - A simulated Winston cone with compression $\alpha = R_1/R_2 = 2$, angle of incidence $\theta = 0°$.

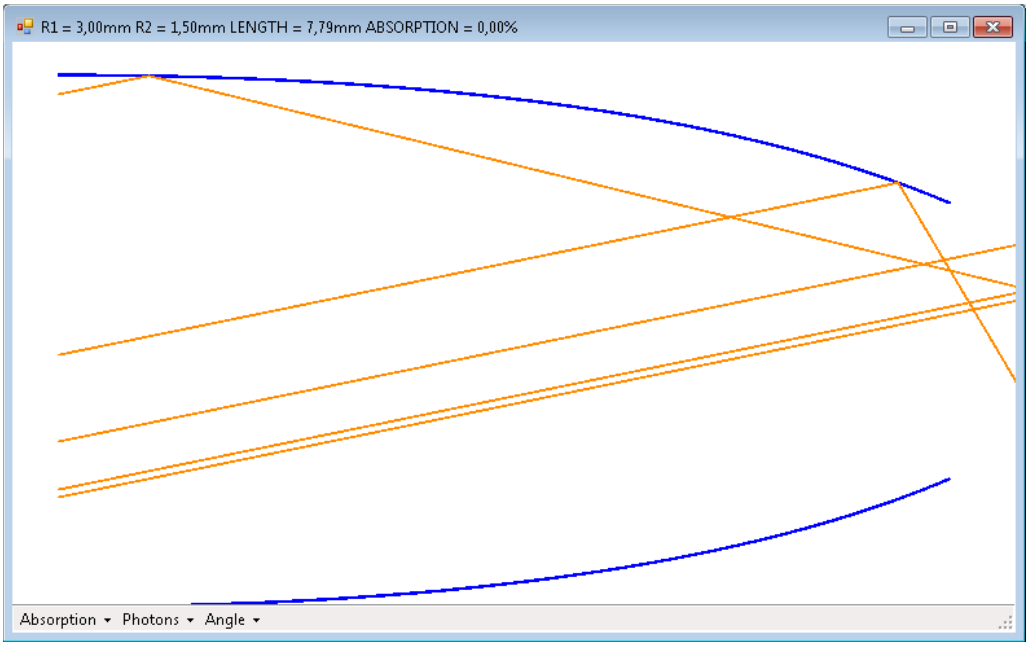

Figure 6.7: Graphical Implementation (Windows 7 C# .NET) - A simulated Winston cone with compression $\alpha = R_1/R_2 = 2$, angle of incidence $\theta = 15°$.

The results of the Winston cone simulation are rebinned to a width of 4° each, starting with -2° ... +2°. The probability $p_{\mathrm{WiCo}}(\theta)$ to detect a photon with an angle θ at the exit of the Winston cone is then given by

$$p_{\mathrm{WiCo}}(\theta) = \frac{N_{\mathrm{BIN}}^{\theta}}{N}, \tag{6.4}$$

where N_{BIN} is the amount of photons within the bin corresponding to θ. This leads to the convolution

$$p = \sum_{\mathrm{bin}} p_{\mathrm{WiCo}}(\theta) \cdot p_{\mathrm{SiPM}}(\theta). \tag{6.5}$$

$p_{\mathrm{SiPM}}(\theta)$ is the probability that has been measured in 5.2. Since $p_{\mathrm{WiCo}}(\theta)$ depends on the geometric compression $\alpha = R_1 \,/\, R_2$, p will likewise differ. The overall efficiency p has been plotted for different compression ratios, see figure 6.8.

An absorption coefficient of $\beta = 10\%$ is commonly known for TYVEK and often used as coatings for reflecting material [25]. At a compression of $\alpha \leq 4$, which means that the bigger radius is 4 times bigger than the smaller ratio, an overall efficiency of greater than 90% is achieved for a vertical angle of incidence.

A random angle $\theta \leq \theta_{\mathrm{max}}$ provides efficiencies of greater 85% and equal, for any compression ratios. As it can be seen in this figure the efficiency decreases with increasing compression ratio. So, it is very important to minimize the compression to achieve higher photon detection efficiencies.

A realistic[1] system of Winston cones and silicon photomultipliers with quite random angles of incidence $\theta \leq \theta_{\mathrm{max}}$ and absorption coefficients of $\beta = 10\%$ is thus applicable.

[1] since reflections within the cone include absorption effect in this simulation

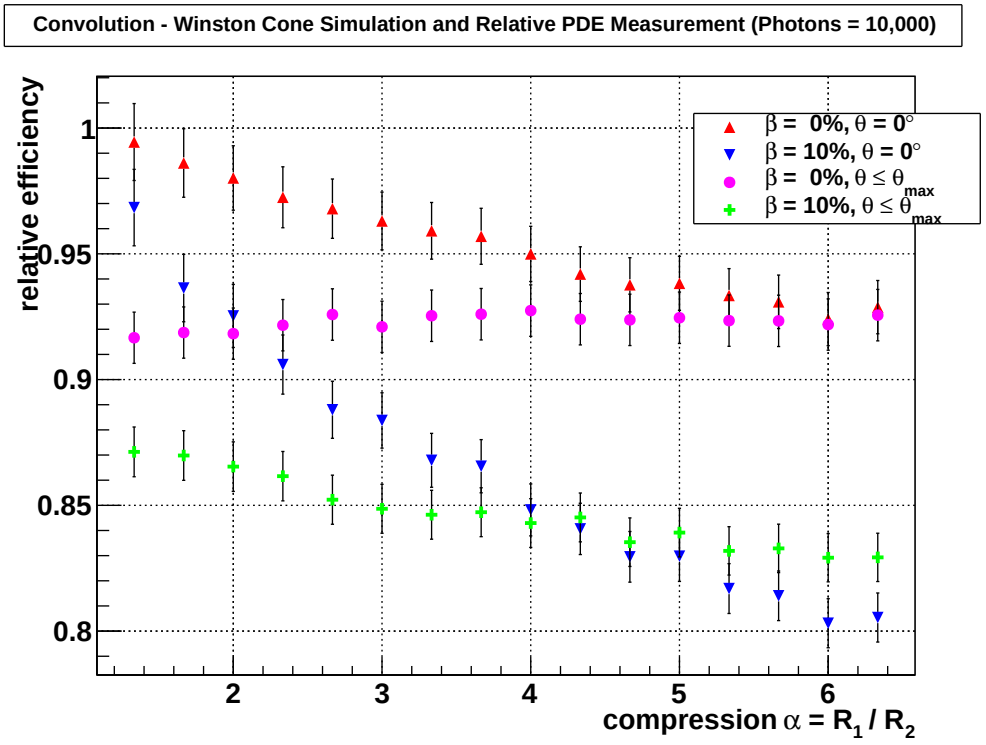

Figure 6.8: Convolution - System of a Winston cone and SiPM: Efficiency relative to absence of Winston cone versus compression. Random incident angle of light $\theta \leq \theta_{\max}$ and $\theta = 0°$. Absorption $\beta = 0\%$ and $\beta = 10\%$.

7. Summary and Outlook

This bachelor thesis has stated that silicon photomultipliers are capable to replace photomultiplier tubes in fluorescence light detectors used in cosmic ray physics.

Although, the thermal noise rate is of the order of 1 MHz at room temperature ($\approx 20\,^{\circ}\mathrm{C}$), the expected photon flux will be even higher. Cooling and thresholds may handle this disadvantage easily.

The relative photon detection efficiency of silicon photomultipliers with respect to the incident angle of light can be accurately described by the Fresnel conditions. These equations describe transmittance and reflection probabilities when light travels from one medium to another with differing refractive indices.

A system combining Winston cones, for light focusing and increasing the sensitive area, and silicon photomultipliers will achieve a relative efficiency of about 94% (depending on the geometric settings of the cone, and angular conditions of the photons), compared to vertical detection of a silicon photomultiplier alone. This implies that these systems are reasonable.

The Auger group at III. Phys. Inst A, RWTH Aachen studies silicon photomultiplier in cooperation with the Laboratory of Instrumentation and Experimental Particles Physics (LIP), Lisbon, Portugal for a future fluorescence detector. A prototype is planned to be manufactured in 2011 for observing ultra-high-energy cosmic ray (UHECR) showers in the Eifel, Germany, called FAMOUS (First Auger MPPC[1] for observation of UHECR showers).

Latest progress, at the time this bachelor thesis has been finished, includes additional characterizations of silicon photomultipliers, e.g. detailed measurements of noise events, like afterpulses and crosstalk.

The absolute photon detection efficiency will also be determined in the future.

Constructions of FAMOUS prototypes are in plan, especially designs of geometric-optical systems.

Compared to the standard fluorescence detector (FD) of the Pierre Auger Observatory, which uses photomultiplier tubes (PMT) for light detection, FAMOUS will be more sensitive for the observation of cosmic ray induced extensive air showers. Thus, the next generation of fluorescence telescopes dawns.

[1] Multi Pixel Photon Counter, synonym for silicon photomultiplier

References

[1] T. Waldenmaier, PhD thesis, Institut für Kernphysik, Karlsruhe, April 2006.

[2] *Kosmische Spurensuche - Astroteilchenphysik in Deutschland*, 2006.

[3] *Auger Website.* http://www.auger.de.

[4] W. Demtröder, *Laser Spectroscopy - Basic Concepts and Instrumentation*, Springer-Verlag, 2 ed., 1998.

[5] D. Renker, Paul Scherrer Institute, Villigen, Switzerland, *Advances in solid state photon detection*, Journal of Instrumentation, 4 (2009).

[6] *Hamamatsu MPPCC - Technical Information.*

[7] *Hamamatsu MPPCC - Catalogue.*

[8] J. Rennefeld, *Studien zur Eignung von Silizium Photomultipliern für den Einsatz im erweiterten CMS Detektor am SLHC*, diploma thesis, III. Phys. Inst. B, RWTH Aachen University, Germany, Febuary 2010.

[9] *Maxim IC DS18B20 - Technical Information.*

[10] *CAEN V965 - Technical Information Manual.*

[11] *Wiener VME-USB - Technical Information Manual.*

[12] *Liblab documentation Website.* http://www.liblab.physik.rwth-aachen.de.

[13] *LeCroy Wavejet 354A - Technical Information Manual.*

[14] *Keithley Sourcemeter 2400 - Technical Information Manual.*

[15] *Lambda/Nemic ZUP-10-20 - Technical Information Manual.*

[16] T. Hermanns, *Aufbau eines Systems für Kühltests zur Qualitätsüberwachung von CMS Silizium-Modulen*, diploma thesis, III. Phys. Inst. B, RWTH Aachen University, Germany, January 2004.

[17] *Kingbright L-7113UVC LED - Technical Information.*

[18] *Dostmann electronics - P470.* private communication.

[19] V. Blobel and E. Lohrmann, *Statistische und numerische Methoden der Datenanalyse*, Teubner, 1998.

[20] C. Piemonte, Divisione Microsistemi, ITC-irst, Povo Di Trento, Italy, *Characterization of the First Prototypes of Silicon Photomultiplier Fabricated at ITC-irst*, IEEE Transactions on Nulear Science, 54 (2007).

[21] M. Petasecca, Italian National Institute of Nuclear Physics, Perugia, Italy, *Thermal and Electrical Characterization of Silicon Photomultiplier*, IEEE Transactions on Nulear Science, 55 (2008).

[22] M. Erdmann, *Experimentalphysik III.* lecture, September 2008.

[23] W. Demtröder, *Experimentalphysik II - Elektrizität und Optik*, Springer-Verlag, 4 ed., 2006.

[24] R. Winston, Optical Society of America, *Cone collectors for finite sources*, Applied Optics, 17 (1978).

[25] J. O. Gichaba, *Measurements of TYVEK Reflective Properties for the Pierre Auger Project*, tech. report, University of Mississippi, Mississippi, USA, August 1998.

Acknowledgements

This bachelor thesis would have not become possible without the assistance of my principals, colleagues, friends and family.

First of all, I like to thank Prof. Dr. Thomas Hebbeker for the chance to prove myself. Discussions in weekly meetings helped me to expand my horizons, not only relating to this topic, but physics in general. Once again, thank you very much.

Dr. Christine Meurer's indefatigable effort, despite her rare spare time, helped me to find my bearings. Thanks for pre-reading my draft of this thesis and for your suggestions in extending my work.

Without *my* graduate student Maurice Stephan, you would not even read this, because it would not have become possible. One could always find a sympathetic ear, day and night.

My colleague Markus Lauscher taught me a lot about Linux systems and C++ programming and I hope that my rewards were in no way inferior.

Thanks to all colleagues in the Pierre Auger group of the III. Phys. Inst. A, RWTH Aachen for their advices towards this thesis and beyond.

A thousand thanks go to my family and friends, who supported me in my hour of darkness.

Many persons simplified my work for the last months at the III. Phys. Inst. A and B, RWTH Aachen. If I list them all, it would depart from tradition. I hope that they will not hold this against me.

Erklärung

Hiermit versichere ich, dass ich diese Arbeit einschließlich beigefügter Zeichnungen, Darstellungen und Tabellen selbstständig angefertigt und keine anderen als die angegebenen Hilfsmittel und Quellen verwendet habe. Alle Stellen, die dem Wortlaut oder dem Sinn nach anderen Werken entnommen sind, habe ich in jedem einzelnen Fall unter genauer Angabe der Quelle deutlich als Entlehnung kenntlich gemacht.

Aachen, den 19. März 2011

Johannes Christian Schumacher